# Regimes identification of the viscous flow past an elliptic cylinder for Reynolds number up to 10000

D. Durante [a] O. Giannopoulou [b] A. Colagrossi [a,c,*]

[a] *CNR-INM INstitue of Marine engineering, 00128, Rome, Italy*

[b] *Department of Mathematics - Sapienza University of Rome, 00185, Rome, Italy*

[c] *ECN / CNRS, École Centrale Nantes, LHEEA Lab., 44300, Nantes, France*

**Abstract**

In the present paper, the study of different regimes arising from the incompressible planar viscous flow past an elliptical cylinder is presented. In order to highlight the effect of the different parameters on the onset of the regimes, two different aspect ratios, 0.10 and 0.40, are considered and the angles of attack span from 0° to 90°, while the Reynolds number is gradually increased from 100 to 10000. The analyses are focused on the lift force acting on the ellipse in order to identify the regime, with a consideration on the vorticity field patterns of the wake fields. The different regimes are investigated and the chaotic behaviour is established through different tools such as the Fourier spectra, phase maps and Poincaré sections. The investigation of the periodic regimes revealed several possible conditions in terms of lift time signal: monochromatic, non-monochromatic and sub-harmonic regimes. In addition, a quasi-periodic time behaviour with an underlying irregular amplitude modulation was also found among the test matrices performed. Increasing the Reynolds number the periodic regimes are lost, giving the place to chaotic behaviour. The numerical solutions are obtained through a vortex particle method called Diffused Vortex Hydrodynamics (DVH). Long time simulations have been carried out in order to guarantee the correct identification of the attained regime.

*Key words:* viscous flows, flow past an elliptical cylinder, Vortex Particle Method

## 1 INTRODUCTION

The mechanism of transition to chaos in a fluid flow is one of still poorly understood topics in fluid mechanics. This transition is dependent on one or more parameters

* Corresponding author: *Tel.: +39 06 50 299 343; Fax: +39 06 50 70 619.*
*Email address:* andrea.colagrossi@cnr.it (A. Colagrossi).

characterizing the system under study. The dynamics of the flow past a circular cylinder at rest in an unbounded plane is an example of a dynamical system dictated by one parameter only, which is the Reynolds number. Conversely, in the case of an elliptical cylinder, the system is defined by three parameters: the aspect ratio, the incidence and the Reynolds number. Because of it, the different regimes of the underlying flow dynamics are expected to be abundant.

From an applicative point of view, the study of such problems is relevant because of the interest in the prediction and control of the forces generated on a body section. The suspended cables of voltage transmission lines, for example, are typically affected by significant vibrations because of the forces generated with the vortex shedding, which can dangerously affect their structural stability. Another example are the thermal wakes, where heat exchangers of elliptical cross-section are shown to be more efficient than the circular ones (see for example Paul et al. [29], Rao and Raju [33]), or even in flow control problems (see Pasquale et al. [28]).

Since the elliptic airfoils exhibit rich flow behaviours, several works can be found in literature, where the effect of the aspect ratio and of the incidence is studied for low Reynolds numbers. One of the earliest experimental investigations related to the flow around an elliptic cylinder dates back to thirty and was the one of Richards [35]. The two-dimensional restriction was obtained by considering a free surface flow (obtained with a moving elliptical cylinder) at low Reynolds number (*i. e.* Re=400) and was mainly devoted to a comparison of the velocity field (in terms of the stream function) with simplified theoretical results. In the seventies, a more detailed experimental campaign was carried out by Taneda [47] in order to study the problem of the boundary layer separation from simple two-dimensional shapes: circular cylinders, elliptic cylinders, flat plates and flexible plates. The free surface streaklines, generated by a 2:1 elliptical cylinder moved by a carriage at different angles of attack, were highlighted through aluminium powder and the connection with the Sears-Telionis separation point was investigated for Reynolds numbers up to 4400.

More recently, Fonseca et al. [13] performed a detailed series of experiments in a vertical hydrodynamic tunnel, devoted to the determination of the shedding frequency for a flow past different profiles. Both thick and slender elliptic cylinders were considered and the Reynolds number was varied up to 2000.

On a slightly different topic, the flow around an elliptic-tip cylinder at high angle of attack was experimentally investigated in the work of Luo et al. [25]. One of the main findings was that when the major axis is transverse to the free stream, it delays the onset of flow asymmetry for high angles of attack.

Nowadays, the increasing numerical abilities coming from new and faster computers allowed to gain a more in-depth on the route to chaos phenomenon coming from the flow past two-dimensional bodies. In order to limit the computing re-

sources, these simulations are generally performed in the reference frame of the body.

Johnson et al. [20] carried out direct numerical simulations of the wake of two elliptical cylinders at low Reynolds numbers (*i. e.* 75−175), varying the aspect ratio. The presence of secondary and tertiary frequencies in the far region of the wake was detected. In Nair and Sengupta [26], two-dimensional unsteady viscous flow around circular and elliptic cylinders was simulated at $Re$=1000, in order to investigate the development of the asymmetry in the wake field. Beside the conclusion that ellipses develop asymmetry earlier than the circular cylinder, the role of discrete roughness in triggering asymmetry was also studied and compared with flow visualization experiments. In Paul et al. [30] the onset of separation was studied for the flow past unconfined two-dimensional elliptical cylinders for various axis ratios and a wide range of angles of attack. A stability analysis exploiting Stuart-Landau equation allowed to calculate critical Reynolds number, marking the transition from steady to unsteady flow regime. The effect of incidence on the unsteady laminar flow past an impulsively started, slender elliptic cylinder was studied numerically for the Reynolds numbers ranging between 25 and 600 in Park et al. [27]. Five distinct flow regimes were identified: two regimes of steady flow and three regimes of unsteady flow.

Finally, among the few papers dealing with the far wake topology, it is the one of Sen and Mittal [41], which investigates the evolution of the far wake of elliptic cylinders with angle of attack varying from 0° to 90° at $Re$=200 and aspect ratios (AR) 0.2, 0.5 and 0.8. The power spectrum analysis of unsteady transverse velocity signal at various stations along the wake centreline is used to study the associated frequencies. The authors found that, in contrast to the decaying nature of primary frequency with incidence, the secondary frequency, not a sub-harmonic of the primary, exhibits a non-monotonic variation.

In the framework of the dynamical systems determined by the flow past airfoils, Pulliam and Vastano [31] wrote one of the pioneering works on this topic. The transition to a chaotic state of the flow past a NACA0012 airfoil was investigated at fixed angle of attack $\alpha = 20°$ and increasing Reynolds number within the range $600 - 3500$. The authors concluded that the transition takes place through several period-doubling bifurcations.

Hopf bifurcations were found also by Jackson [19], which studied the transition from steady to periodic solution of an ellipse with aspect ratio 0.5 and varying angle of attack ($0° - 90°$). A similar strategy of investigation is also present in Saha et al. [40] for two-dimensional flow past a square cylinder.

Other studies on the same topic were carried out by Liu et al. [24] and recently by Bose and Sarkar [4] and Kurtulus [22, 23], where the effects of the thickness and of the angle of attack on the wake topology were investigated in terms of vorticity

fields. Two symmetric airfoils were considered, a NACA0002 and a NACA0012 at a fixed Reynolds number ($Re$=1000) and varying incidence. The author concluded that, for each airfoil, there are five different modes identified through the arrangement of the shed vorticity and the time behaviour of the lift force, depending on the angle of attack. The transition of the dynamical system among the different modes manifests through period-doubling and period-quadrupling bifurcations, before attaining the chaotic regime.

Recently, Rossi et al. [39] used a vortex particle method for a NACA0010 airfoil at angle of attack $\alpha = 30^\circ$ and the same modes of Kurtulus [23] were found. However, only period-doubling bifurcations were observed in the transitions sequence to chaotic regime.

One of the last works on the topic was the one of Durante et al. [12], where the flow past a NACA0010 airfoil at $Re$=1000 was numerically investigated, using the same particle vortex method of Rossi et al. [39] for $0^\circ \leq \alpha \leq 90^\circ$. Very detailed simulations accurately characterised the route to chaos, when the incidence reaches 27°. Poincarè sections of the lift maxima and phase maps related to lift force were exploited and the presence of period-tripling, period-6 and period-12 bifurcations were found for the first time.

In the present paper, the study of the flow past an elliptical cylinder at aspect ratios 0.10 and 0.40 is performed for different angles of attack, spanning in the range $0^\circ - 90^\circ$. The Reynolds number is varied from 100 to 10000. The present investigation is devoted to studying in terms of the lift force, the effect of the thickness and of the angle of attack when the Reynolds number is increased.

A particular advantage of the use of the lift coefficient is that it is strictly connected with the time variation of the momentum of the vorticity over the whole fluid domain (see section 3 and appendix B). Therefore, it is expected that significant changes on the wake topology will impact on the lift force signal. Different techniques are instead exploited by other authors for the investigation of the long-lived Lagrangian structures shed in the flow field (see Serra and Haller [42], Serra et al. [43], Sun et al. [46]).

Starting from the time behaviour of the lift coefficient, the corresponding Fourier spectra are derived, as well as the phase-space maps and the related Poincarè sections. The consideration of the lift as a phase space variable may be also found in Khalid and Akhtar [21], Rossi et al. [39] and Durante et al. [12].

The numerical model used in this study is a vortex particle method, called Diffused Vortex Hydrodynamics (DVH). It belongs to the general class of Lagrangian methods used for the numerical simulations of unsteady viscous flow problems (see *e.g.* Cottet et al. [10]), where the fluid is discretized into vortex elements. These methods have the definite advantage of eliminating the pressure calculation, of not requiring any stability condition and the implicit fulfilment of the far field boundary

conditions. Furthermore, this approach yields an accurate evaluation of both near and far fields. The numerical algorithm, outlined in the appendix A, was recently developed and validated on numerous benchmark tests (see Rossi et al. [36, 37, 38], Colagrossi et al. [7], Durante et al. [11] and Giannopoulou et al. [14]). In the numerical simulations considered, high spatial resolutions are used for the near field around the body, as well as for the wake region.

Furthermore, computations were carried out for such a long time, that the identification of each regime may be assumed as correctly attained.

The paper is organised as follows: in Section 2, a summary of the different test matrices used throughout the paper is reported and the corresponding parameters are indicated; in Section 3, an outline of the interaction mechanism between the shear layers is presented for circular and elliptical cylinders; in Section 4, the conditions for which the steady regimes appear are discussed; in Section 5, a wide description of the onset of different periodic regimes is carried out, pointing out the numerous natures of this behaviour (*i.e.* monochromatic, non-monochromatic and sub-harmonics); in Section 6, the chaotic regime is detailed; finally, in Section 7, the global trends in terms of mean lift coefficients are outlined for every test matrix. Conclusions are offered in Section 8.

## 2 Problem description and test matrix

The geometry considered for the test cases is an ellipse with two different aspect ratios, where or the Reynolds number or the angle of attack are the varying parameters. The aspect ratio AR is $b/a$ where $a$ and $b$ are the major and minor axes respectively; the Reynolds number is defined with the major axis as $Re = Ua/\nu$, where $U$ is the free stream velocity and $\nu$ is the kinematic viscosity. The Reynolds number spans an interval from 100 to 10000, while the angle of attack may vary from $0^\circ$ to $90^\circ$.

The test matrix is composed by seven series, which were carried out with one parameter varying for each of them. In table 1, the series and their corresponding parameters are outlined while a more complete list of every simulation performed and the related regime found will be addressed in table 2.

The 121 simulations have been carried out with a Vortex Particle Method (VPM) called Diffused Vortex Hydrodynamics (DVH). It is based on a Chorin's splitting technique and outlined in appendix A. Since only the vortical part of the flow field is discretized, this kind of VPM allows high resolution outcomes with reduced computational costs in comparison with other numerical methods.

The maximum Reynolds number was limited to 10000, because the transition to a

| Test case | AR | $\alpha$ | Re |
|---|---|---|---|
| N1 | 0.40 | 0° | 200 - 10000 |
| N2 | 0.40 | 20° | 100 - 10000 |
| N3 | 0.10 | 0° | 500 - 10000 |
| N4 | 0.10 | 20° | 100 - 10000 |
| N5 | 0.10 | 30° | 100 - 2000 |
| N6 | 0.10 | 0° - 90° | 2000 |
| N7 | 0.10 | 0° - 90° | 250 |

Table 1
Test matrix. The series N5 was already discussed in Rossi et al. [39] and is here reproposed for the sake of completeness.

chaotic condition appears in this range. The study of higher Reynolds numbers is left for future works and is, at the moment, out of our scope.

The more severe issue related to the present investigations is the necessity to perform a large number of detailed simulations for a very long time in order to be confident with the identification of the different regimes. In fact, as discussed in section 5, a transitory condition could be attained for a significant time interval, before the onset of one or more bifurcations that move the system toward a different regime. Besides, a detailed description of the wake field can be also important in view of the regime evaluation (as stressed in the work of Durante et al. [12] and Kurtulus [23]) and typical finite volume/finite differences methods suffer of severe numerical diffusion, so that the wake vorticity is hardly conserved unless very fine grids are exploited, with a significant impact on the computational costs even in 2D frameworks. Because of the above considerations, the adoption of a VPM seems the best choice for these kinds of studies.

Finally, we are interested in a 2D restriction for the present study primarily because in a 2D framework the phenomena investigated are more rich from the dynamical systems point of view. Indeed, as shown in Durante et al. [12], in the Reynolds number regime investigated in this work, the complex 2D vortex dynamics observed would be hardly detectable on a 3D framework. In fact the vortex stretching along the transversal direction disrupts the two-dimensionality of the coherent structures. It is worth noting that the extension to a 3D analysis would require high computational costs which makes the present investigation too demanding (see Durante et al. [12] and appendix A.1).

The present 2D approach is applicable in real life when low Froude number free surface flows are considered, or in atmospheric stratified flows but the interested reader can refer to the review study of Boffetta and Ecke [3] for a more comprehensive discussion.

## 3 Outline of the shear layers interaction in the flow past an elliptic cylinder

Historically, the flow past a circular cylinder was one of the oldest and better investigated topics, the importance of which relying on a simple shape able to trigger complex wake patterns, when the Reynolds number or the ratio diameter/spanwise length are varied. In a 2D framework, a strong link exists between the force time signals and the related vorticity field, when a typical flow regime is observed. The shear layers interaction at $1000 \leq Re \leq 10000$ ($Re$ is here the Reynolds number referred to the diameter of the cylinder) deserves some remarks for pointing out the link between the near wake behaviour and the lift time signal in a simple case, where the typical parameters considered for an ellipse (*i. e.* thickness and angle of attack) are neglected.

As outlined in Graziani and Bassanini [17] and in Riccardi and Durante [34] the global forces $\mathbf{F}_b$, acting on the body, are related to the first momentum of the vorticity field:

$$\mathbf{M}(t) = \int_{\Omega} \mathbf{r}\, \omega(\mathbf{x}, t)\, dV \tag{1}$$

where $\Omega$ is the fluid domain which extend from the body surface $\partial\Omega_B$ up to the infinity. The relation with the forces $\mathbf{F}_b$ is given by:

$$\mathbf{F}_b = \rho \left[ \frac{d\mathbf{M}^{\perp}}{dt} - \Gamma \boldsymbol{U}^{\perp} \right] \tag{2}$$

where $\Gamma$ is the total circulation in the flow field and $\rho$ the fluid density, while the symbol $\mathbf{v}^{\perp}$ is the perpendicular operator (*i.e.* if $\mathbf{v} = (v_1, v_2)$, then $\mathbf{v}^{\perp} = (-v_2, v_1)$). If the flow field starts form a rest condition, the circulation is zero at initial time and it remains zero for all the times, so that the straight relation holds:

$$\mathbf{F}_b = \rho \frac{d\mathbf{M}^{\perp}}{dt}\,. \tag{3}$$

The Equation (3) links the vorticity field to the forces, therefore, the time behaviour of $\mathbf{F}_b(t)$ is expected to be connected with the wake topology. For example, a periodic behaviour of the lift force is often traceable in a well organised regular wake with large vortex dipoles (see *e.g.* Kurtulus [23] and in Durante et al. [12]). Conversely, a chaotic time signal of the lift force is more associated with a chaotic distribution of vorticity in the wake. In section 5.3 we will discuss more in depth this point.

The present paper is based on a vortex particle approach, described in appendix A, so that, by using the description of the vorticity field indicated in formula (A.4), the forces acting on the body are directly evaluated from the wake circulation distribution:

$$L = \rho \frac{d}{dt} \left( \sum_{j=1}^{N_v} x_j \Gamma_j \right) \qquad D = \rho \frac{d}{dt} \left( \sum_{j=1}^{N_v} y_j \Gamma_j \right) \tag{4}$$

where $L$ and $D$ are the lift and the drag acting on the body, respectively. This approach allows us to take into account all the vorticity field in the calculation of the forces, such making the analysis of the lift signal more meaningful for the system state description. Furthermore, we stress to the reader that the forces evaluated through the first momentum of the vorticity are always superimposable to those calculated through the integral on the body surface (using the procedure elucidated in Colagrossi et al. [8]) so that the Equation (3) is always checked.

The dynamics in the near wake, where separation occurs, is dominated by the shear layers stability and by their mutual interaction, as pointed out by Zdravkovich [50]. Although the wake shed by an airfoil in a lifting condition can be investigated theoretically (see Riccardi and Durante [34]), the separated flows coming from airfoils in stalled configurations, as well as from the flow past bluff bodies, is typically studied with experimental or numerical approaches. Even though some theoretical attempts started with Goldstein [16], a convincing analytical development on this topic is still lacking, being the modelling of the shear layers and of their dynamics too complex for meaningful simplifications. However, in recent years some effort in this sense was done by Serra and Haller [42], Serra et al. [43]. Being the boundary layer over an immersed body a source of vorticity, flows past blunt bodies may be challenging to reproduce thoroughly (especially in the near wake), in particular when the increasing of the Reynolds number induces a strong filamentation of the shed vortical structures and a severe instability of the shear layers, as visible in Figure 1. Disregarding the increasing complexity of the near and far wake dynamics due to a further increasing of the Reynolds number, described *e.g.* in Singh and Mittal [45] and Durante et al. [11], the scope of the present section is to emphasize the role of the shear layers interaction in the definition of the flow regime even when the simplest blunt body is taken into account.

The different behaviour of shear layers, when the Reynolds number (referred to the diameter of the cylinder) varies from 1000 to 10000, is depicted in Figure 1. Although at $Re = 1000$ the near wake shows large vortical structures with evident dissipation at just an half of diameter from the cylinder and low interaction between shear layers, for higher Reynolds numbers the flow field radically changes with layers roll up and fragmentation, as shown at $Re = 10000$. This behaviour is dually observed in the lift force Fourier spectra, shown in Figure 2. The weak layers interaction at $Re = 1000$ induces a clearly periodic behaviour and discrete signal peaks are recognized (corresponding to the different harmonics of the periodic signal), whereas a period-doubling mechanism leads to the numerous discrete peaks of $Re = 2000$ spectrum. For higher Reynolds numbers the complex shear layers interaction marks the transition from regular to chaotic regime, with the Fourier spectra passing from discrete to continuous. These regimes are known in literature as *low subcritical* and are well described in Zdravkovich [50] and Durante et al. [11].

Because the surface curvature affects the rate of turbulent kinetic energy production

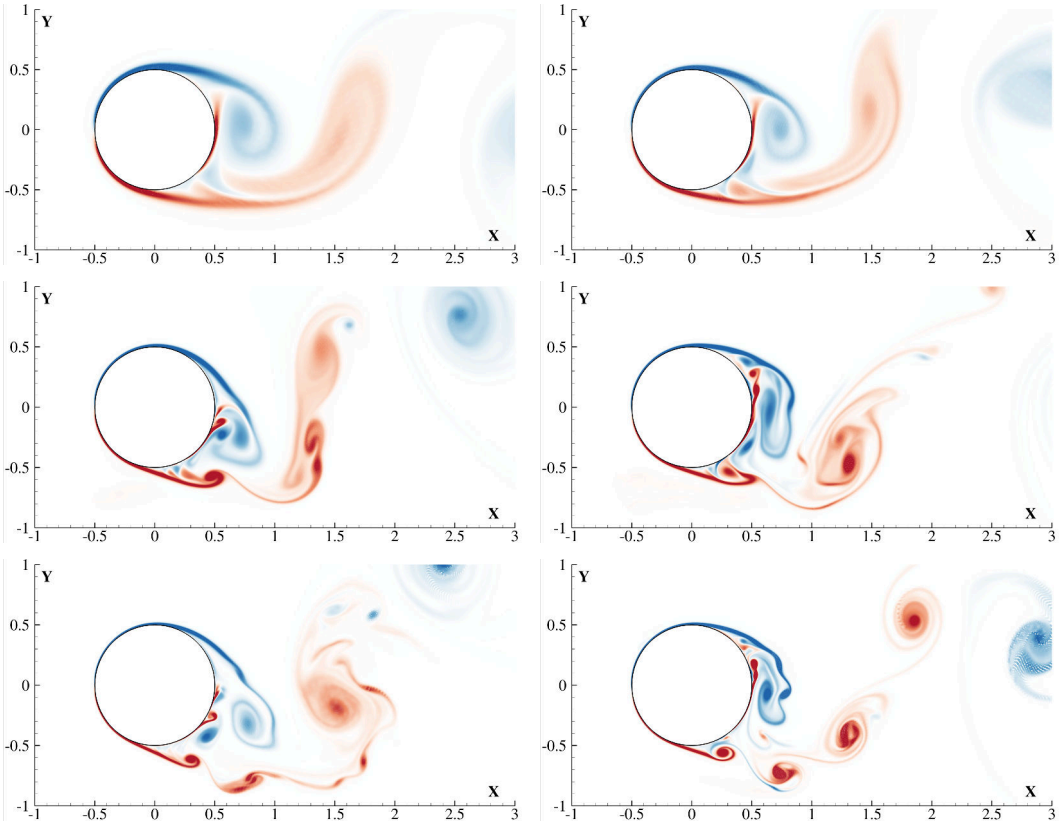


Figure 1. Non-dimensional near wake vorticity $\omega^*$ contours for the flow past a circular cylinder at maximum lift conditions. The contours are scaled from blue to red. From top left to bottom right: $Re = 1000$, 2000, 5000, 6000, 9000, 10000. For $Re = 1000$ the contour range is in $\pm 20$, for $Re = 2000 - 6000$ in $\pm 25$ and for $Re = 9000$ and $Re = 10000$ in $\pm 30$. Different ranges are used to highlight the local interaction of the shear layers.

within the boundary layer (as remarked in the pioneering work of Ramaprian and Shivaprasad [32]), the effect of the aspect ratio is taken into account by considering two elliptic shapes of different thickness.

In the left column of Figure 3, the vorticity fields generated by a thick and a thin ellipse at $Re = 5000$ without incidence are depicted. The proximity of the shear layers shows a low interacting dynamics so that the near flow field appears remarkably periodic. [1] The thick ellipse, with a minor/major axes ratio $b/a = 0.4$, exhibits a retarded separation with rolled layers that eventually form a large dipoles wake arrangement and induce a periodic force time behaviour. The shape thinning at aspect ratio $b/a = 0.1$ enforces the prevention of boundary layer separation in a final laminar periodic regime (see Zdravkovich [50]) and steady forces. An aspect ratio different from 1 inevitably leads to adding a new parameter because of the presence of the angle of attack at which the profile is set. The Figure 3 shows in the right column both profiles at $\alpha = 20°$ and the intense shear layers interaction which in-

[1] Here, we want to give only an overview of the problem; an in depth detail on this point will be offered in section 5.3.

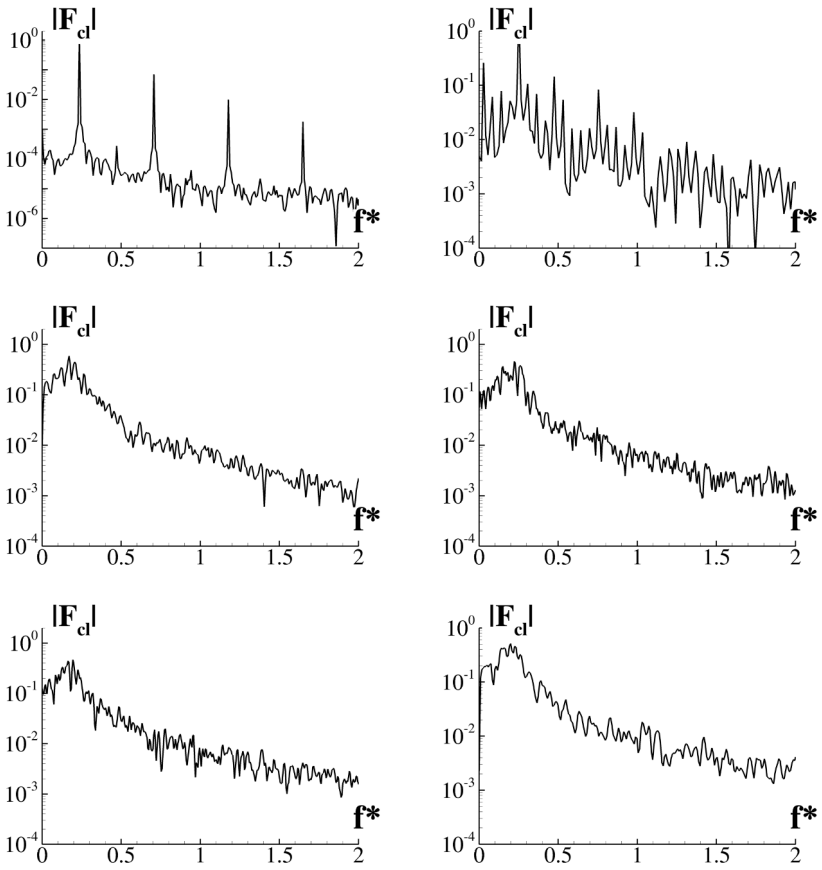


Figure 2. Fourier transform of the lift coefficient time signals referred to the cases in Figure 1. From top left to bottom right: $Re$ = 1000, 2000, 5000, 6000, 9000, 10000.

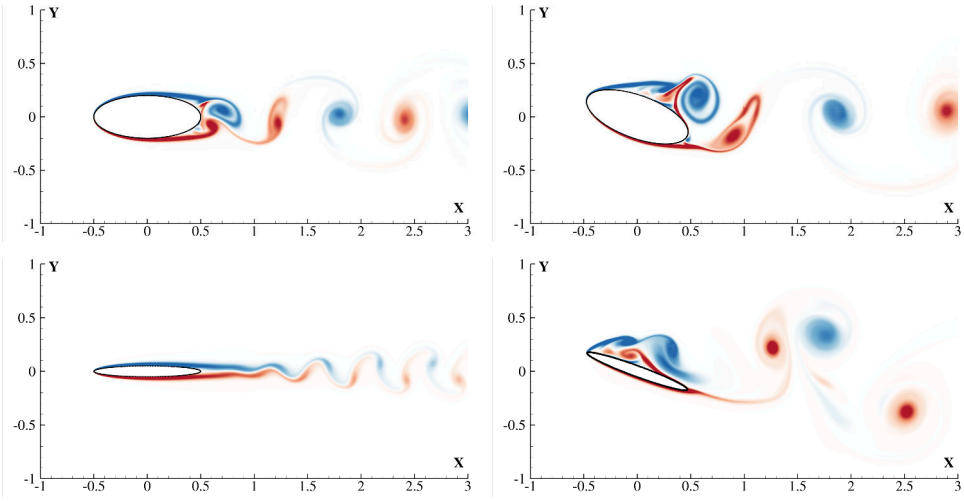


Figure 3. Effect of thickness and of angle of attack on the shear layers interaction. **Top-left**: $\alpha = 0°$, $Re = 5000$. **Top-right**: $\alpha = 20°$, $Re = 5000$. **Bottom-left**: $\alpha = 0°$, $Re = 5000$ **Bottom-right**: $\alpha = 20°$, $Re = 4000$. The non-dimensional vorticity contours are scaled from blue to red in the range $|\omega^*| \leq 20$ with the exception of the bottom-right, where $|\omega^*| \leq 25$.

duces, at the same Reynolds number, a chaotic vortex field in the wake. It should be underlined that a lower aspect ratio is characterised by higher curvature at leading and trailing edges (which became geometric singularities in the limit of a flat plate). At the leading edge the shear layer separates easier for $b/a = 0.1$, being the high curvature responsible for higher instability, as shown in the lower-right frame of Figure 3. The visible rolling up of the upper shear layer is described in literature as "*transition eddies*" and are typically observed in the low-subcritical regime of the flow past a circular cylinder (see Durante et al. [11] and Zdravkovich [50]) but for higher Reynolds numbers (around $10^4$).

## 4 Steady regime

The steady regime of the flow past an immersed body is defined as the condition for which the forces acting on it are constant in time. When dealing with a circular cylinder, Zdravkovich [50] correctly divides the *creeping flow* regime, where the viscous forces are such dominant that all disturbed regions of the flow field remain laminar and the flow is firmly attached to the surface of the circumference, from the *near wake* regime where a separation exists. Instead of the potential solutions, which can be easily found (see Batchelor [2]) analytically, a creeping flow solution is not directly deducible, as remarked by the Stokes paradox. For $5 \leq Re \leq 30-48$, the presence of separated shear layers creates a stable recirculation region within the near wake, which elongates with the increment of the Reynolds number and becomes unstable in the far wake (*i. e.* $\simeq 10 - 20c$), because of the fluctuation of

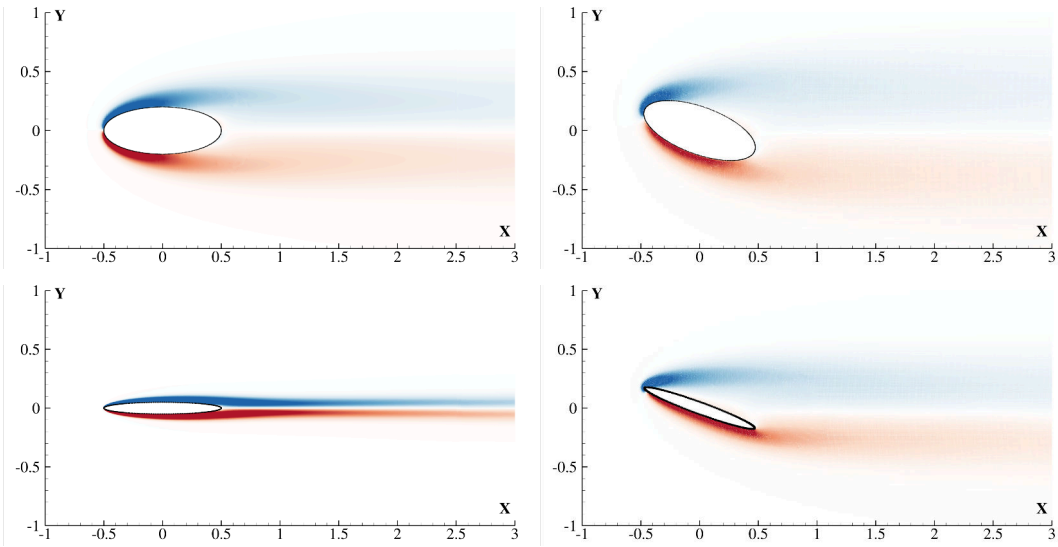


Figure 4. Vorticity contours (from blue to red and $|\omega^*| \leq 10$) for steady separation regimes in four configurations. **Top-left**: $Re = 200$, $b/a = 0.4$ and $\alpha = 0°$, **top-right**: $Re = 100$, $b/a = 0.4$ and $\alpha = 20°$. **Bottom-left**: $Re = 3000$, $b/a = 0.1$ and $\alpha = 0°$, **bottom-right**: $Re = 200$, $b/a = 0.1$ and $\alpha = 20°$.

the confluence point (for further details, see Zdravkovich [50]). For the Reynolds numbers between 50 and 200, the flow is still classified as steady, remaining the forces on the cylinder rather constant, but the Navier-Stokes equations exhibit a periodic solution in terms of vorticity field. The classification of this kind of regime is *laminar periodic*, according to Zdravkovich [50].

In the case of elliptic cylinders, the creeping flow solution is still valid for low Reynolds numbers. Indeed, in the pioneering work of Shintani et al. [44], the matched asymptotic expansions method is exploited for obtaining the complete description of the flow field around an ellipse at low Reynolds number and $\alpha = 90°$. Beside very few analytical works on this topic, a complete analysis of the Reynolds number range at which the transition toward the steady separation occurs still lacks.

Depending on the aspect ratio of the ellipse and on the angle of attack, the increasing of the Reynolds number leads to the formation of two distinct shear layers similarly to the cylinder steady separation regime. Unlike the cylinder case, the Reynolds numbers range at which the flow past the ellipse remains within a stable regime may be very wide.

In Figure 4 four different configurations are shown. At $\alpha = 0°$ the lower the thickness, the higher the Reynolds number of steady separation. Indeed at $b/a = 0.4$ the flow remains steady at $Re = 200$, but switches to periodic for slightly higher Reynolds values (at $Re = 500$ the solution becomes periodic, see section 5). Conversely for $b/a = 0.1$ the solution persists in this regime for $Re \approx 3000$.

A slight increment of angle of attack (lower than 10°) poorly affects the maximum Reynolds number at which the steady regime persists. A further increase of the incidence strongly reduces the Reynolds number range, making the effect of the

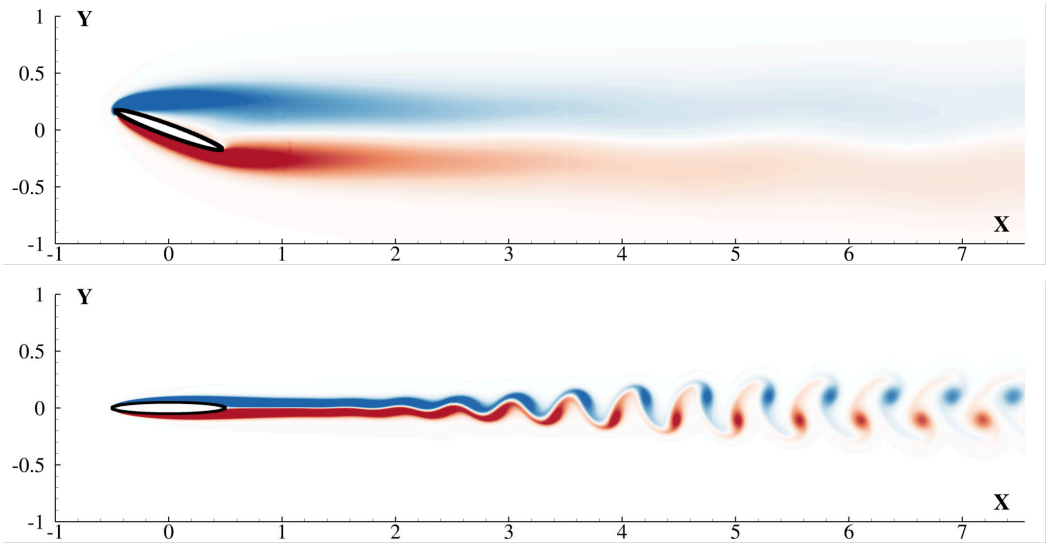


Figure 5. Vorticity contours (from blue to red and $|\omega^*| \leq 4$) for laminar periodic wake and $b/a = 0.1$ at $\alpha = 20°$ and $Re = 200$ (**top**) and $\alpha = 0°$ and $Re = 4000$ (**bottom**).

thickness negligible. In Figure 4 the thick ellipse at $Re = 100$ and the thin at $Re = 200$ are shown. At $\alpha = 20°$, the steady condition is soon lost for $Re > 100 - 200$, moving toward a periodic one.

The laminar periodic wake regime, observed in the flow past a circular cylinder for $38 - 40 < Re < 180 - 200$, is here found for the thin ellipse more evidently for lower angles of attack. In Figure 5 two cases are shown. At $\alpha = 20°$ the wake becomes slightly oscillating at $Re = 200$, but the perturbations on the forces, although existing, are too weak to classify these latter as periodic. Conversely, at $Re = 300$ this behaviour will be more evident, as it will be discussed later. At $\alpha = 0°$ the flow remains in steady regime within a wider interval. At $Re = 4000$, sketched in the bottom plot of Figure 5, the wake shows perturbations in the shear layers, starting about 2 chords away from the ellipse and weakly amplifying in the far field. The shed dipoles are still too weak to have a measurable effect on the time variation of the forces acting on the ellipse, so that this case is still classified as steady.

For the thick ellipse, the laminar periodic regime never appears in the cases analysed so that or this regime is too unstable to persist or it will for $100 < Re < 200$ at $\alpha = 20°$ and $200 < Re < 500$ at $\alpha = 0°$.

However, it can be concluded that the thinning of the thickness plays a non trivial role in the increasing the stability of this regime.

From the Equation (3), in the steady regime, the first vorticity momentum is a linear function of time:

$$\sum_{j=1}^{N_v(t)} x_j(t)\,\Gamma_j(t) = -\frac{\bar{L}}{\rho}\,t \qquad \sum_{j=1}^{N_v(t)} y_j(t)\,\Gamma_j(t) = \frac{\bar{D}}{\rho}\,t$$

where $\bar{D}$ and $\bar{L}$ are respectively the constant drag and lift (the latter is not null when the incidence is different from zero, *i.e.* there is no symmetry with respect to the $x$-axis).

## 5 Periodic regime

When the incidence or the Reynolds number increase, the shear layers, initially not interacting in the near wake, are subjected to the trigger of an early instability that definitely leads to the onset of a periodic regime, which becomes typically visible through a von Kármán vortex shedding. Depending on the ellipse thickness, as well as on the angle of attack, the periodic regime deserves special attention because of numerous different conditions that may arise. In particular, as shown for a NACA profile in Durante et al. [12] and in Rossi et al. [39], the forces time behaviour (typically the lift force) may appear as a pure monochromatic, when the parameters

are close to a steady condition, but it evolves in a periodic non-monochromatic behaviour and may be eventually subjected to period bifurcations, as the angle of attack or the Reynolds number increases, thus preluding to a chaotic transition (see also Pulliam and Vastano [31], Kurtulus [23] and Durante et al. [12]).

In the following, the different periodic regimes related to the variation of the incidence as well as of the Reynolds number for thick and thin ellipse will be investigated. As in the former section, the Reynolds numbers considered for every case, as well as the angles of attack, are the maximum ones (among the simulated) at which that regime appears (see table 2).

### *5.1 Monochromatic signal*

Moving from the steady, in some cases the periodic regime early manifests with a monochromatic behaviour of the global forces over the immersed body. In the cylinder case, the forces time signal becomes monochromatic for $Re \approx 100$ as discussed in Durante et al. [11], this being actually related to the regular shedding observed in the near wake with low interacting vortex dipoles. A similar condition is here observed for the ellipse in different configurations. In Figure 6 the vorticity fields show a regular shedding, also for high Reynolds numbers when the angle of attack is zero. Indeed, in the top-left frame the thick ellipse at $Re = 1500$ and $\alpha = 0°$ is depicted, whereas the thin one at $Re = 7000$ at the same angle of attack is shown right down. The effect of the thickness is to stimulate the shear layers separation, so that the thinning tends to suppress it in analogy with a flat plate. The vortex shedding is then allowed to remain within a stable regime, where the global forces acting on the body are not only periodic but even monochromatic. The corresponding Fourier transforms of the lift signals are depicted in Figure 7, where a main signal peak, corresponding to the shedding frequency, is found. For the $b/a = 1$ the shedding frequency where the monochromatic behaviour is attained is about 0.163 at $Re = 100$ (see Durante et al. [11], Zdravkovich [50]), while for $b/a = 0.4$ it is found at 0.59 and for $b/a = 0.1$ to 2.26. This forward shifting of the maximum shedding frequency at which this regime appears, is the obvious consequence of the increasing Reynolds number at which it is found. Conversely, the amplitude lowers from 0.33 of the cylinder to $0.33 \times 10^{-2}$ of the thin ellipse, this meaning that the shedding mechanism becomes faster and of lower intensity. As remarked in the steady regime, the higher the incidence the lesser the stability of the regime. Indeed, from the right column of Figure 6, it can be observed that the shape influence on the persistence of monochromatic periodic regime is rather negligible. The maximum Reynolds numbers where it was found at 20° were $Re = 200$ for thick and $Re = 300$ for the thin ellipse. The shedding frequency for these cases, being the Reynolds number very similar, is not dramatically different: 0.3 for the thick ellipse and 0.45 for the thin one. On the log scale used for the plot of the transforms, a second peak for $f^* = 0.89$ is found in the thin case, although ten times

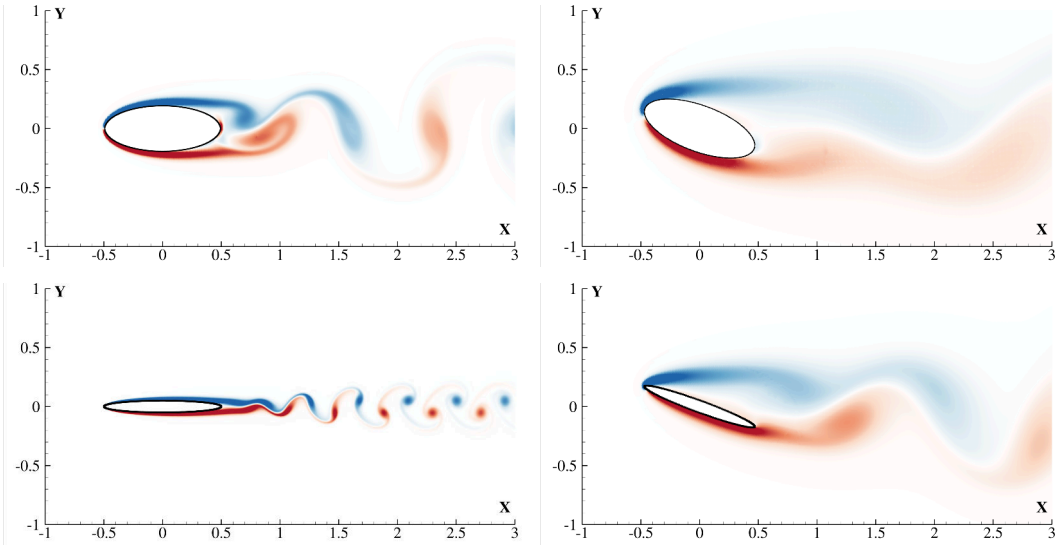


Figure 6. Vorticity contours (from blue to red) for monochromatic periodic regime at $\alpha = 0°$, $Re = 1500$ and $b/a = 0.4$ (**top-left** , $|\omega^*| \leq 15$); $\alpha = 20°$, $Re = 200$ and $b/a = 0.4$ (**top-right**, $|\omega^*| \leq 10$); $\alpha = 0°$, $Re = 7000$ and $b/a = 0.1$ (**bottom-left** , $|\omega^*| \leq 15$); $\alpha = 20°$, $Re = 300$ and $b/a = 0.1$ (**bottom-right**, $|\omega^*| \leq 10$)

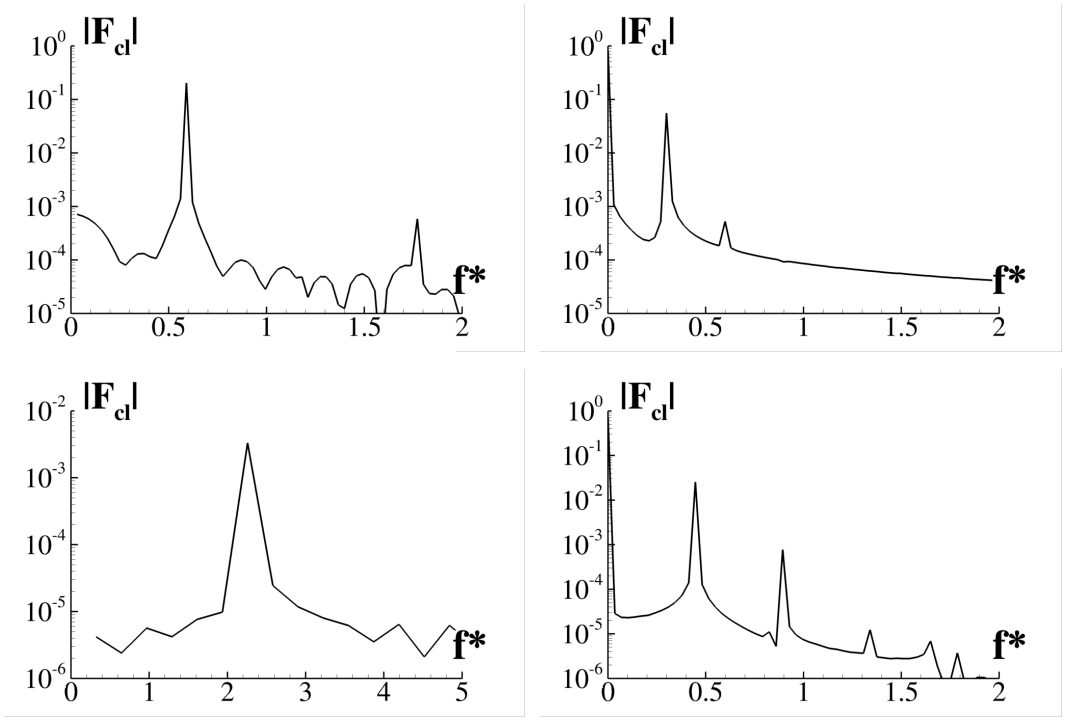


Figure 7. Fourier transform of the lift coefficient time signals referred to the cases in Figure 6. $\alpha = 0°$, $Re = 1500$ and $b/a = 0.4$ (**top-left** ); $\alpha = 20°$, $Re = 200$ and $b/a = 0.4$ (**top-right**); $\alpha = 0°$, $Re = 7000$ and $b/a = 0.1$ (**bottom-left** ); $\alpha = 20°$, $Re = 300$ and $b/a = 0.1$ (**bottom-right**). The non-dimensional frequency is $f^* = c/(tU)$

lower in amplitude, so that a monochromatic behaviour may be still assumed.

In the series N6 and N7, where the angle of attack is varied according the table 1, the monochromatic behaviour was identified for $\alpha = 10^\circ$ at $Re = 2000$ and at $\alpha = 20^\circ$ for $Re = 250$, where the spectrum is very similar to the one depicted in the bottom-right frame of Figure 7. This clearly confirms that the effect of the Reynolds number increasing is to lower the angle of incidence at which this regime appears. It is interesting that just at 15° of the series N6, the lift is already non-monochromatic. If the monochromatic behaviour persists over the 10°, it can within the narrow range $10^\circ - 15^\circ$ of incidence at $Re = 2000$.

In the periodic monochromatic regime the lift $L$ and the drag $D$ forces can be expressed as a simple sinusoidal function:

$$L(t) = \bar{L} + L_0 \cos(2\pi f\, t + \phi_L)\,, \qquad D(t) = \bar{D} + D_0 \cos(4\pi f\, t + \phi_L)\,,$$

where $f$ is the shedding frequency, $L_0$ and $D_0$ are, respectively, the lift and drag amplitudes, and $\phi_L$ and $\phi_D$ are the corresponding phases. As well known, due to the alternating vortex wake, if the oscillations in lift force occur at the frequency $f$, the ones of the drag force occur at twice the frequency $f$.

According to Equation (4), the first vorticity momentum is:

$$\sum_{j=1}^{N_v(t)} x_j(t)\,\Gamma_j(t) = -\frac{\bar{L}}{\rho}\,t - \frac{L_0}{2\pi\, f\,\rho}\,\sin(2\pi f\, t + \phi_L)$$
$$\sum_{j=1}^{N_v(t)} y_j(t)\,\Gamma_j(t) = \frac{\bar{D}}{\rho}\,t + \frac{D_0}{4\pi\, f\,\rho}\,\sin(4\pi f\, t + \phi_D)$$

Therefore, as in the steady regime, also in this special case an analytic expression, with few parameters, of the first order moment of the vorticity is available.

### *5.2 Non-Monochromatic signal*

The onset of the periodic regime is characterized by the organization of the wake in a well ordered arrangement with big vortex patches emanating from the body. A similar regime was found for the cylinder at $Re = 1000$ and depicted in Figure 1, where the alternate rolling up of the shear layers induces a local strain, which force the shed vorticity in detaching regularly and in coherent patches that ultimately form large and low interacting dipoles in the wake. The Fourier transform (Figure 2) shows a discrete-peaks spectrum, where every other peak corresponds to harmonics of the first one in a typical periodic fashion.

Passing to the ellipse, a behaviour similar to the cylinder is observed for the thick shape. Looking at the top row of Figure 8 a similar shedding mechanism is found

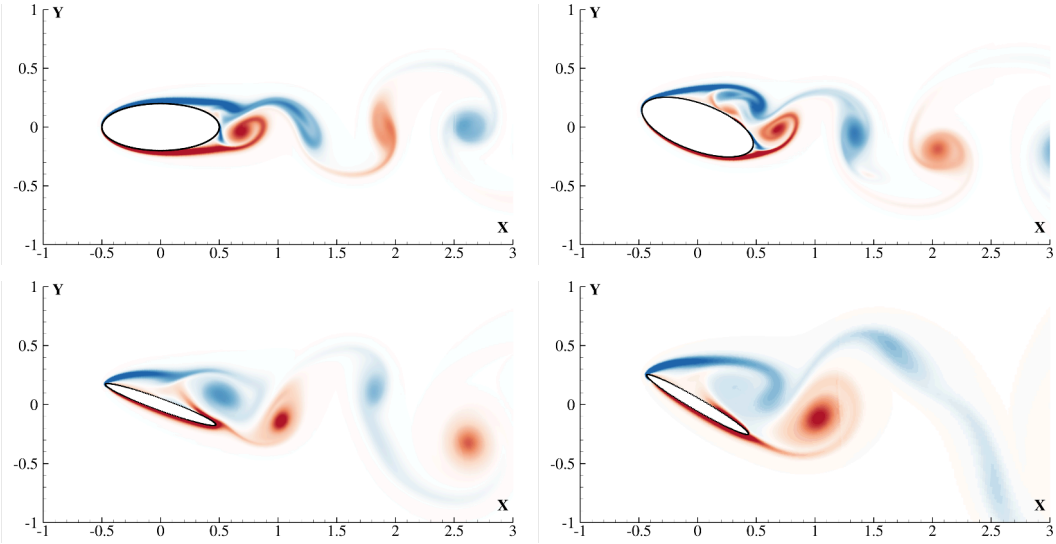


Figure 8. Vorticity contours for periodic regime at $\alpha = 0°$, $Re = 2500$ and $b/a = 0.4$ (**top-left** , $|\omega^*| \leq 15$); $\alpha = 20°$, $Re = 3000$ and $b/a = 0.4$ (**top-right**, $|\omega^*| \leq 20$); $\alpha = 20°$, $Re = 1400$ and $b/a = 0.1$ (**bottom-left** , $|\omega^*| \leq 20$); $\alpha = 30°$, $Re = 900$ and $b/a = 0.1$ (**bottom-right**, $|\omega^*| \leq 15$)

for $\alpha = 0°$, whereas it seems more complex when the incidence increases ($\alpha = 20°$) and the alternate rolling up of the shear layers suffers of a poor stability due to their mutual interaction. The vorticity is now shed in stretched filaments, which finally reorganise in large dipolar structures persistent in the wake field up to 20-30 chord lengths. The lift coefficient time behaviour is depicted in the top row of Figure 9 where, after a short transient, the regime appears with a regularly oscillating signal.

The Fourier transform (Figure 10) depicts, coherently, the same scenario. The principal peak related to the shedding frequency is followed by higher harmonics lower peaks of about two order lower magnitude, thus indicating that, despite of the high Reynolds numbers involved ($Re = 2500$ for $\alpha = 0°$ and $Re = 3000$ for $\alpha = 20°$), the signals are very similar to a sinusoid. Although a nearly periodic behaviour for the thick ellipse at 0° was found up to $Re = 10000$, the only case after $Re = 1500$ where a typical spectrum associated to a clearly periodic behaviour manifests is $Re = 2500$, the other regimes revealing a quasi-periodic nature, discussed in section 5.3. Conversely, the thin ellipse cases show periodicity after longer transients, where eventually a different regime may be established.

The bottom row of Figure 8 shows a shedding mechanism similar to the airfoil one observed in Durante et al. [12], Rossi et al. [39], with the rolling up of the lower layer that directly detaches and is shed in the wake poorly interacting with the upper one, which is in turn interested by an higher stretching. This dynamics appears strikingly more regular in this case, with a discrete peak Fourier transform which describes a periodic signal far from a sinusoid. The higher frequencies show peak amplitudes with a low decay, with the second harmonics component of the same order of the first one. In contrast with the thick ellipse, in this case the system

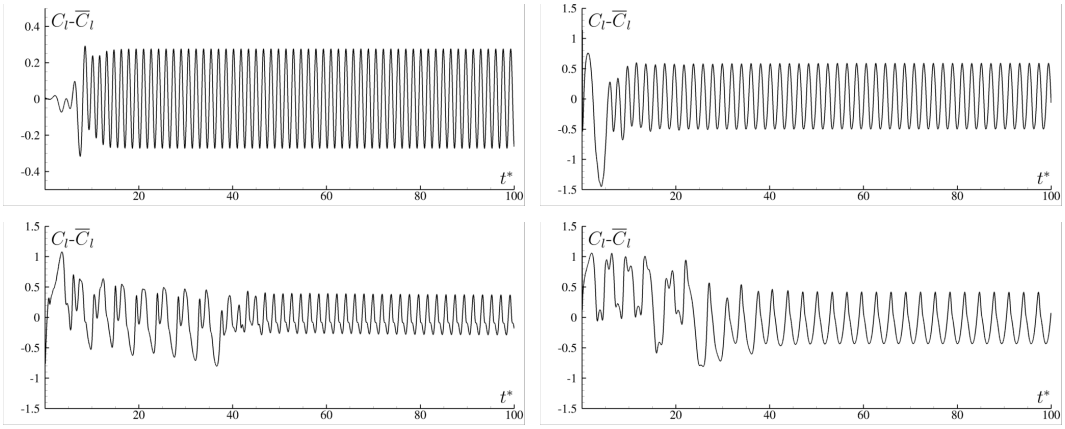


Figure 9. Lift coefficients time signals referred to the cases in Figure 8. $\alpha = 0°$, $Re = 2500$ and $b/a = 0.4$ (**top-left** ); $\alpha = 20°$, $Re = 3000$ and $b/a = 0.4$ (**top-right**); $\alpha = 20°$, $Re = 1400$ and $b/a = 0.1$ (**bottom-left** ); $\alpha = 30°$, $Re = 900$ and $b/a = 0.1$ (**bottom-right**). The mean values have been subtracted for the sake of clearness. The non-dimensional time is $t^* = tU/c$

reaches the periodic regime with greater stability issues. In particular, the Figure 9 clearly shows that for $\alpha = 20°$ and $Re = 1400$ the $b/a = 0.1$ shape manifests

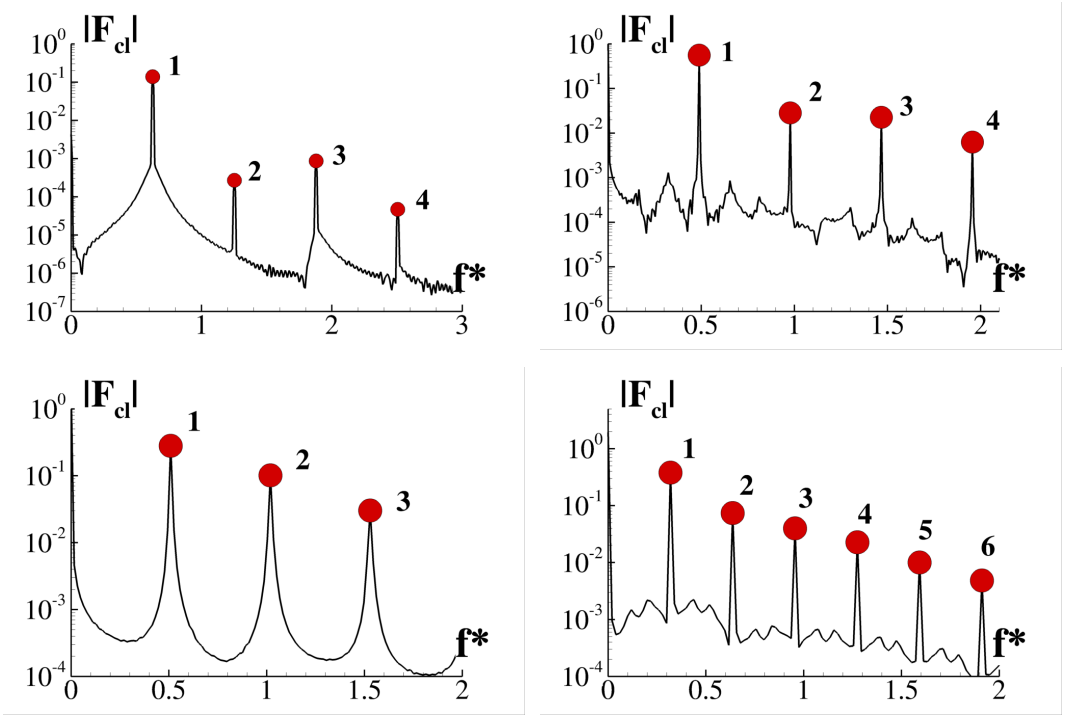


Figure 10. Fourier transform of the lift coefficient time signals referred to the cases in Figure 8. The peaks corresponding to the harmonics of the signals are marked with red dots and with the corresponding numbers. $\alpha = 0°$, $Re = 2500$ and $b/a = 0.4$ (**top-left** ); $\alpha = 20°$, $Re = 3000$ and $b/a = 0.4$ (**top-right**); $\alpha = 20°$, $Re = 1400$ and $b/a = 0.1$ (**bottom-left** ); $\alpha = 30°$, $Re = 900$ and $b/a = 0.1$ (**bottom-right**). The non-dimensional frequency is $f^* = c/(tU)$

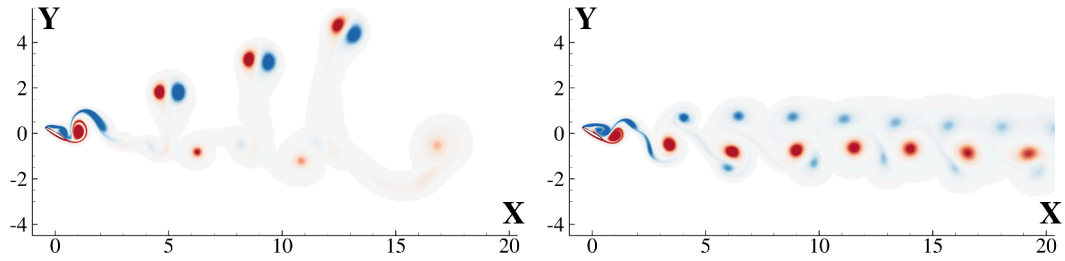


Figure 11. Vorticity contours ($|\omega^*| \leq 5$) for periodic regime at $\alpha = 30°$, $Re = 900$ and $b/a = 0.1$. **left** $t^* = 32.5$, **right** $t^* = 97.25$

.

a more complex regime with a double peak in the lift signal before reaching (for $t^* > 50$) a regular periodic behaviour. In terms of the wake filed, this means a different arrangement of the vorticity field, as sketched in Figure 11, where the case $b/a = 0.1$, $Re = 900$ and $\alpha = 30°$ is shown. In the left frame a time instant falling within the transient is depicted, whereas in the right frame the vorticity field at regime is drawn. As evident, the transient is interested by energetic dipoles moving upwards and bending in the stream direction (similarly to the Mode IIIb observed for the NACA airfoil in Durante et al. [12]), but a different and compact arrangement is observed at the regime.

The interesting conclusion that can be grasped from this analysis is that the onset of a stable periodic regime is mainly dependent on the ellipse thickness rather than the angle of attack.

### *5.3 Quasi-periodic behaviour*

The force behaviour for the thick ellipse at $\alpha = 0°$ has revealed some non trivial aspects that deserve a special section for a brief discussion.

Despite the regular periodic behaviour described in the previous section for $Re = 2500$, in the interval $2000 \leq Re \leq 10000$ the other simulations performed have shown a different behaviour, where clear peaks emerge from a very irregular spectrum resembling a chaotic regime, described later in section 6. If the spectra depicted in Figure 12 are much similar to the periodic kind discussed in section 5.2 for $Re = 2000, 3000$ and $4000$, from $Re = 5000$ a basic continuous spectrum can be appreciated and the periodic behaviour seems the carrier signal on which a chaotic modulation overlaps. These signals are known as *quasi-periodic* (see also Bailador et al. [1]).

From the frequency ratio between the harmonic peaks, we found that they are in a sequence 1-3-5 ... This means that we have a time signal which is a periodic function with half-wave symmetry. In order to show the chaotic underlying nature of the lift modulation, the case $Re = 7000$ was considered as an example. Despite the

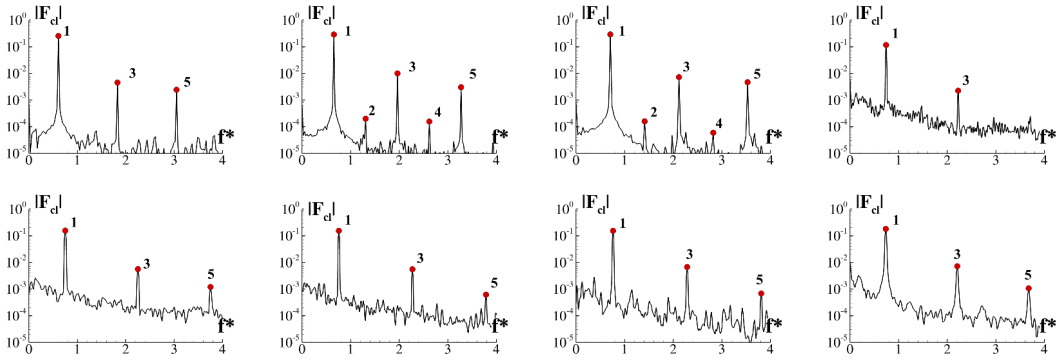

Figure 12. Fourier transform of the lift coefficient time signals referred to the cases $\alpha = 0°$ and $b/a = 0.4$. From left to right on **top**: $Re = 2000$, $Re = 3000$, $Re = 4000$ and $Re = 5000$. From left to right on **bottom**: $Re = 6000$, $Re = 7000$, $Re = 8000$ and $Re = 10000$. The non-dimensional frequency is $f^* = c/(tU)$ The peaks corresponding to the harmonics of the signals are marked with red dots and with the corresponding numbers.

clearly periodic shedding of vortex dipoles depicted in the top frame of Figure 13, the nonlinear local interaction of upper/lower boundary layers leads to the lift signal fluctuations drawn in the bottom frame of the same figure. By exploiting the property of half-wave symmetry, the original signal was added to the half-period shifted one and the irregular part is highlighted. Respect to the oscillation amplitude of the carrier signal, which is about 0.3, this second signal is ten times lower in amplitude and possesses almost the same frequency. This means that the is actually a chaotic amplitude modulation and this finally explains why we see a typical periodic vortex shedding. The chaotic nature is actually related to the fluctuations on the intensity of vortex patches released in the flow field and not to the shedding frequency. This regime deserves further investigations however, for the sake of brevity, it will be matter of future works.

### *5.4 Sub-harmonic modes*

Whenever after a parameter variation, the force periodic time signal is interested by a frequency modulation of the carrier harmonics with a stable persistence, we talk about a sub-harmonic regime. When dealing with dynamical systems, this condition typically represent the forerunner of a chaotic cascade, as remarked in Durante et al. [12], Kurtulus [23], Pulliam and Vastano [31]. From now on, we will make use of two classical instruments of chaotic systems analysis: the Poincarè sections, obtained as the local maxima (for regime condition, *i. e.* the flow field state attained after the transient) of the lift signal drawn in the ($\ddot{C}_l$-$C_l$) plane, and the phase maps, which represent the trajectories in the plane ($C_l$-$\dot{C}_l$) of the time signal. The usual technique to construct the Poincarè section is by first reconstructing the phase-space using the time-delay embedding method. Then the sections are found by taking intersections of this phase-space with a transverse plane (see for example Wolf et al. [49], Saha et al. [40]). Instead of using this method, here the phase-space is recon-

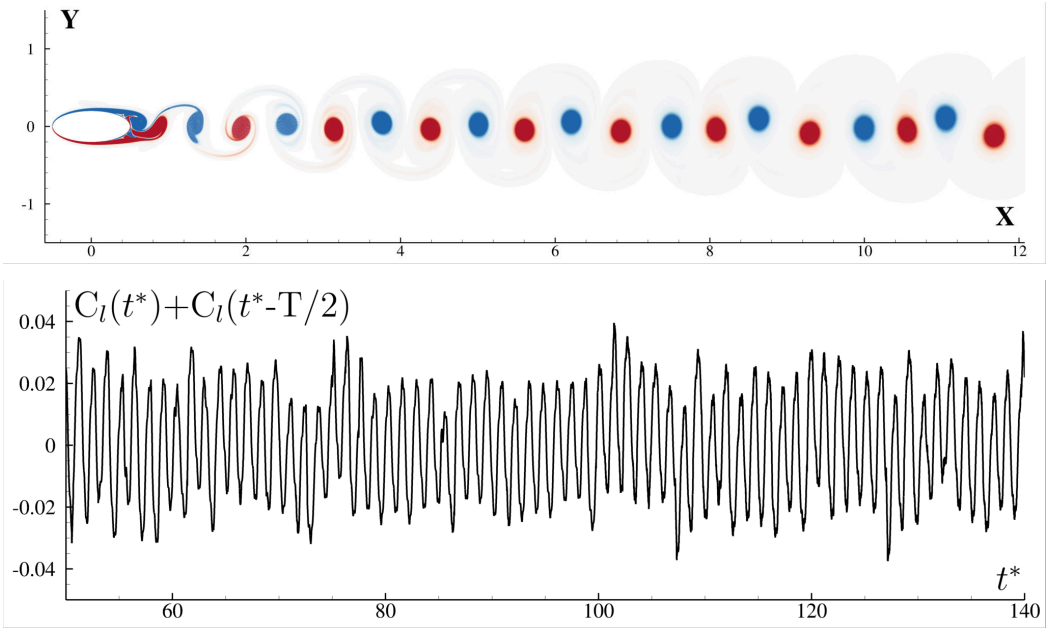


Figure 13. On **top**: vorticity field for $Re = 7000$, $\alpha = 0°$ and $b/a = 0.4$. The vorticity is contoured from blue to red for $|\omega^*| \leq 5$. On **bottom**: chaotic part of the lift signal for the same case, obtained exploiting the half-wave symmetry of $C_l$. The non-dimensional time is $t^* = tU/c$

structed using the differential phase-space embedding since with this technique an existence of the Poincaré section is guaranteed, according to Gilmore [15]. To this end, first $C_l, \dot{C}_l, \ddot{C}_l$ are used to reconstruct the phase space. Then intersections of it with the surface given by $\dot{C}_l = 0$ where $\ddot{C}_l < 0$ will give the Poincaré section.

The best way for collecting all the cases studied and highlighting these modes is to refer to the table 1 where a synoptic sketch of all the simulation performed is given. We decide to start with the series N4, which considers a thin ellipse (*i. e.* $b/a = 0.1$) at $\alpha = 20°$ and varying Reynolds number. As shown in Figures 8,9 and 10 of section 5.2, the case $Re = 1400$ represents a typical periodic regime, the Fourier transform of which resembles a classic discrete peaks spectrum.

By increasing the Reynolds number, the lift signal changes abruptly. As sketched in Figure 14, at $Re = 1450$ the $C_l$ is clearly affected by a low frequency modulation and the discrete peak spectrum of $Re = 1400$ is now interested by numerous sub-harmonic peaks, not sharp yet.

When the Reynolds number rises up to $Re = 1500$, the sub-harmonic peaks become more energetic and well clear in the spectrum, this being the effect of a radical change in the lift signal. From the second frame (from the top), four peaks are visible in the lift period and this directly reflects on the spectrum shape. For every sharp peak in the spectrum of $Re = 1400$, shown in Figure 10, four peaks appear and this bifurcation represents a *period-quadrupling*. In literature, Pulliam and Vastano [31] observed numerous period-doubling bifurcations for a NACA0012 at 20°, in

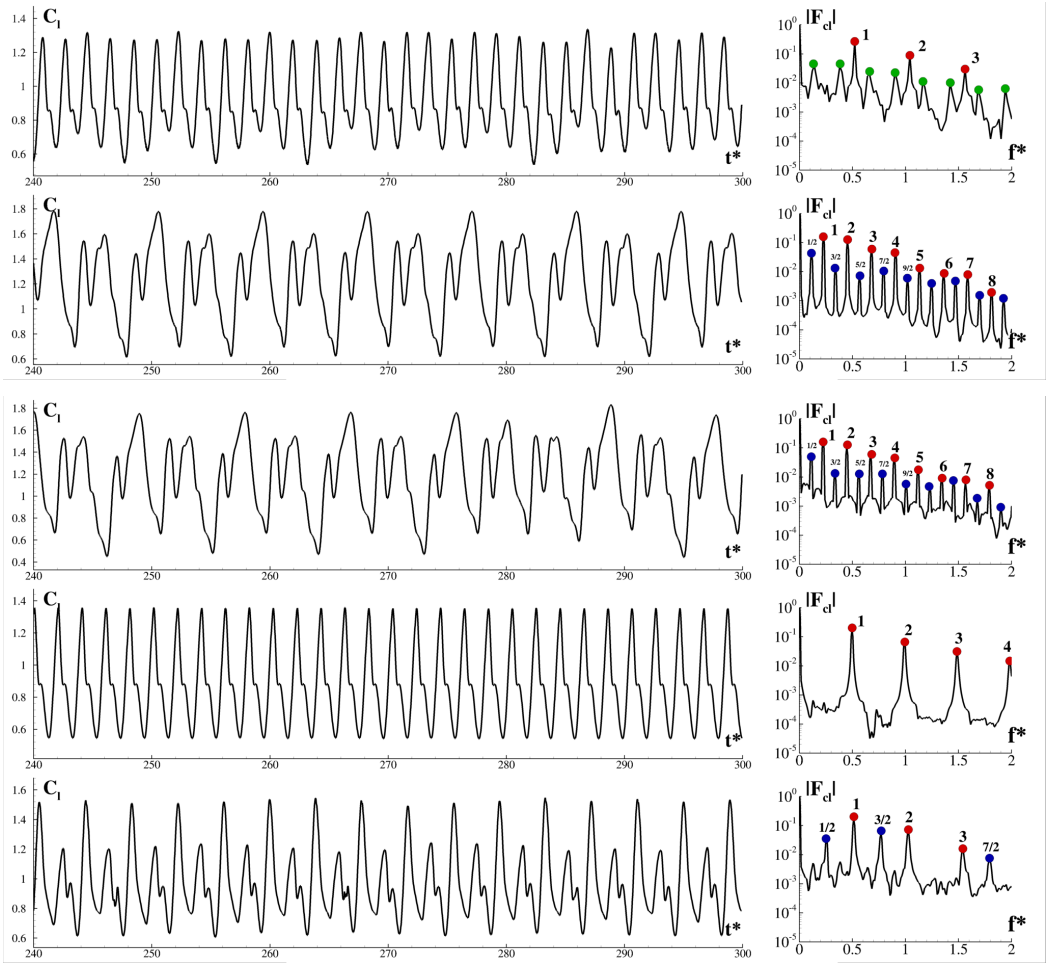


Figure 14. Lift signals (**left**) and corresponding Fourier transforms (**right**) for $b/a = 0.1$ and $\alpha = 20°$ at varying Reynolds number. From top to bottom: $Re = 1450$, $Re = 1500$, $Re = 1600$, $Re = 1700$ and $Re = 1800$. The non-dimensional time is $t^* = tU/c$, the non-dimensional frequency is $f^* = c/(tU)$. The peaks corresponding to the harmonics of the signals are marked with red dots and with the corresponding numbers. With blue dots the peaks of commensurable sub-harmonics are marked and the corresponding fraction is indicated. The non commensurable sub-harmonics peaks are marked with green dots.

particular for Reynolds number changing from 1400 to 1525, 1575 and 1580 and argued that this bifurcations were the evidence of a route to chaos. Actually in Durante et al. [12] numerous period-tripling bifurcations were found before the chaos inception for a NACA0010 at varying angles of attack. To the authors' knowledge, a period-quadrupling was never documented for the flow past an airfoil.

The Poincarè sections and the phase maps in Figure 15 may help to better understand this phenomena. Although for $Re = 1450$ the Fourier analysis does not offer any particular insight beyond an unclear modulation, the Poincarè section reveals an evident period-doubling identified through the two groups of points well separated in the plane. It is worth to remark that a typical doubling, with sharp discrete peaks in the Fourier transform, would have produced two groups of very clustered

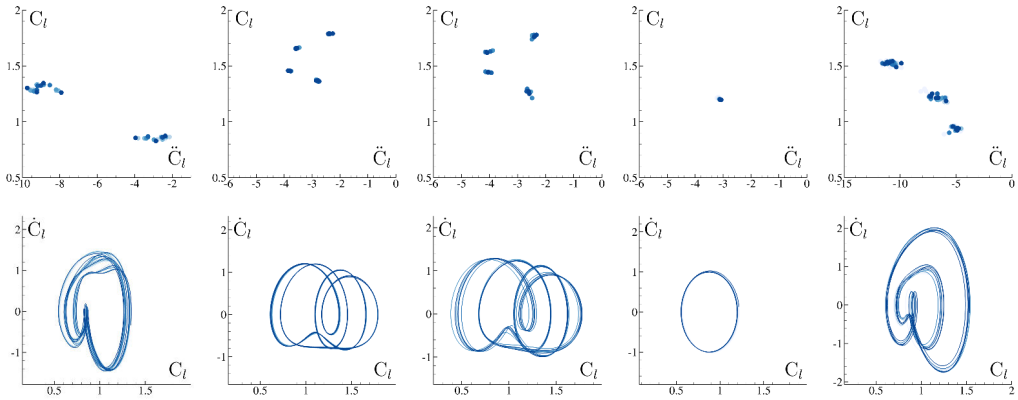

Figure 15. Poincarè sections (**top**) and phase maps (**bottom**) for $b/a = 0.1$ and $\alpha = 20°$ at varying Reynolds number. From left to right: $Re = 1450$, $Re = 1500$, $Re = 1600$, $Re = 1700$ and $Re = 1800$. The points, as well as the phase lines, are contoured with non-dimensional time in order to highlight the points and the curves clustering with the time.

points, because of the time sequence of two groups of maxima where every group is (rather) associated to one single value. In this case, the low frequency modulation of the signal induces some scattering of the two groups of maxima.

Similarly, the phase map shows a big orbit, clue of a periodic signal carrier, and a second little one knotted within the first which is again the mark of a doubling, as discussed in Durante et al. [12], Pulliam and Vastano [31].

As discussed before, at $Re = 1500$ the signal and Fourier transform suggest the onset of a period-quadrupling and this is evidently highlighted by the Poincarè section where four distinct maxima groups are visible. Unlike the case $Re = 1450$, now the signal carrier is more regular and the phase map reveals four distinct orbits where also the internal knotted ones are of similar dimensions of the external, thus remarking the four different maxima found in the time signal period.

The case $Re = 1480$ is more complicated and interesting to discuss, but we will deal with it later for making the present discussion more comfortable to the reader.

At $Re = 1600$ the situation does not change much from the former with a lift signal shape, and coherently the Fourier spectrum, very similar to the $Re = 1500$ case. The passage to $Re = 1700$ marks a new come back to a regular periodic condition with a period halving primarily evidenced by a lift time signal resembling the 1400 (see Figure 9), a Fourier spectrum with discrete peaks at almost the same frequencies of $Re = 1400$ (the gap is less than the 3%) and a Poincarè section with a single point (or, more precisely, very clustered points). As expected, the phase map shows a single nearly circular orbit, which can be easily demonstrated that becomes a perfect ellipse when the signal is a sinusoid (*i.e.* the function and its first derivative are orthogonal).

The last case investigated within the N4 series, after which the system becomes

chaotic, is the $Re = 1800$ which is drawn in the last row of Figure 14. From the time signal, three maxima are distinguishable in the period although one of them is significantly lower in amplitude respect to the other two. In the dynamical system context, this behaviour is classified as *period-tripling* when three peaks for every one of the carrier appear in the Fourier spectrum. However, the harmonic analysis does not give a clear support to this classification and it is better to move toward the analysis in Figure 15. The Poincarè section and the phase map confirm the presence of a period-tripling where three orbits are found (it is worth noting that the inner, littler than others, corresponds to the little maximum observed in the time signal) and three clusters of points are visible. We want to underline again the importance of the Poincarè sections and phase maps covered for the classification the different bifurcations of the reference time signal.

The case $Re = 1480$, skipped during the former discussions, is commented more in-depth below. The interest comes from the singular behaviour of the system in this case, which experiences a significant instability before reaching a regime condition. A deeper insight comes from the visualization of the vorticity fields that corroborate the direct link between the lift signal and the circulation distribution in the wake.

Figure 16 depicts different time ranges of the lift force signal and the corresponding Fourier transforms. In the bottom frame the regime condition is sketched and it appears evidently periodic with the already seen and discussed discrete peak spectrum. As shown in corresponding plot of Figure 17, the regime condition corresponds to a compact arrangement of the wake field (which resembles the Mode IV regime of Durante et al. [12]) and the periodic behaviour of the lift force is remarked by a single point in the Poincarè section and a single orbit in the phase map. As mentioned before, the regime condition is preceded by numerous bifurcations in time. From the earliest range $40 \leq t^* \leq 70$, the signal is characterized by two period maxima and a Fourier spectrum with the peak frequencies doubled in number respect to the regime condition. The wake field in Figure 17 is characterised by large dipoles emanating upwards and bending streamwise similarly to the transient regime of thin ellipse at $\alpha = 30°$ and $Re = 900$ seen in Figure 11. In the phase map two big orbits are visible, although not sharply, as well as two point clusters in the Poincarè section. From the Fourier transform, a period-doubling bifurcation is observed when $80 \leq t^* \leq 130$ and the signal itself exhibits a period where five maxima are traceable, although two of them are very close to each other. From the Figure 17, a qualitative change in the vorticity shed is observed. Large dipoles are still emanating upwards but most of them tend to bend in the opposite direction of the stream. Similarly, the Poincarè section now reveals five point clusters, where two of them are very close in straight agreement with the time signal and the phase map shows four distinct orbits, doubled respect to the former time range, in analogy with the Fourier spectrum.

The things change when $150 \leq t^* \leq 200$ where a period halving recasts the spectrum is a similar configuration of the first time range. The orbits in the phase map

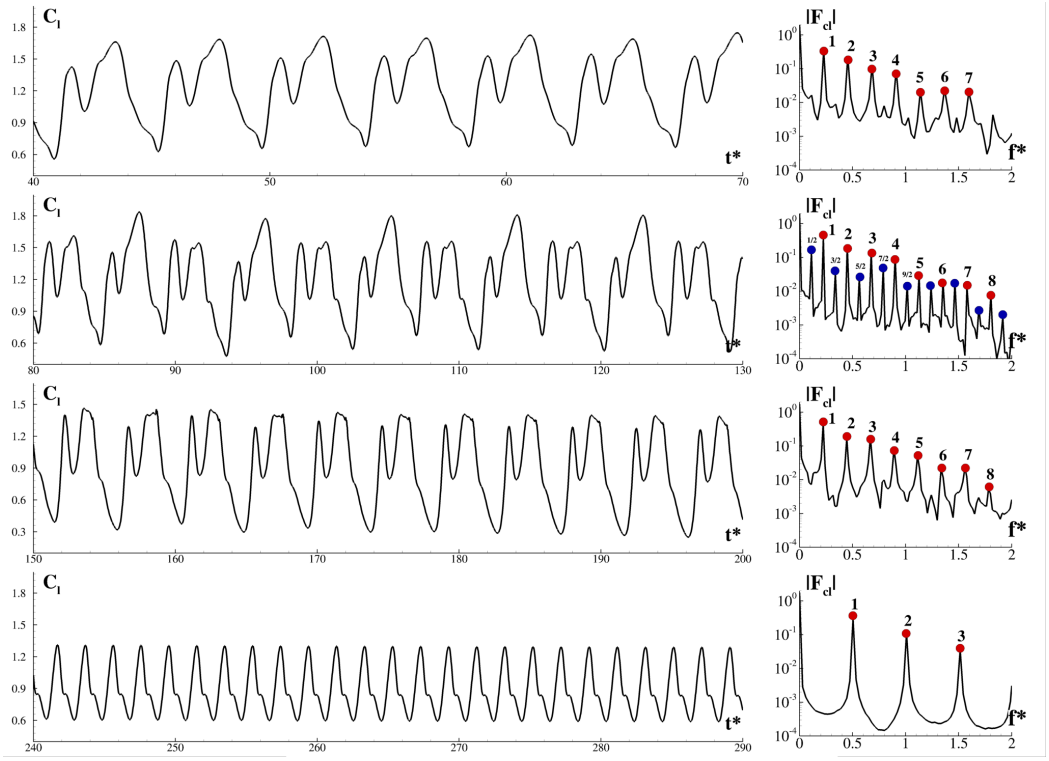


Figure 16. Lift signals (**left**) and corresponding Fourier transforms (**right**) for $b/a = 0.1$ and $\alpha = 20°$ at Reynolds number 1480 and different time ranges. The non-dimensional time is $t^* = tU/c$, the non-dimensional frequency is $f^* = c/(tU)$. The peaks corresponding to the harmonics of the signals are marked with red dots and with the corresponding numbers. With blue dots the peaks of commensurable sub-harmonics are marked and the corresponding fraction is indicated.

are now two and the Poincarè section shows two groups of maxima. The wake transforms again and the dipoles are so bent that the wake becomes more compact. Finally, for $t^* > 200$, a new period halving brings the system to its regime condition.

It is worth to stress that, according to our investigation, this condition persists at least up to $t^* = 300$, but we have not a final proof that it indefinitely does. However, when this compact arrangement of the wake was found in different cases it seems to be very stable (see, for example, the case shown in Figure 11 or the perturbation study of the case $\alpha = 29.1°$ of Mode IV in Durante et al. [12]). Furthermore, it is useful to notice that the mean value of the lift force strictly depends on the wake topology. Indeed, as already found and discussed in Rossi et al. [39], the lower the compactness of the wake the higher the mean lift, which passes from 1.23 of the top frame of Figure 16 to the 0.88 of the bottom. A comparison with the case $b/a = 0.4$ at the same angle of attack is useful in order to investigate the effect of the thickness on the onset of sub harmonic regimes. As depicted in Figure 18, by increasing the Reynolds number the time signals exhibit evident modulations. Conversely to the $b/a = 0.1$ the signal shape does not radically change remaining fairly regular and without bifurcations during the transient.

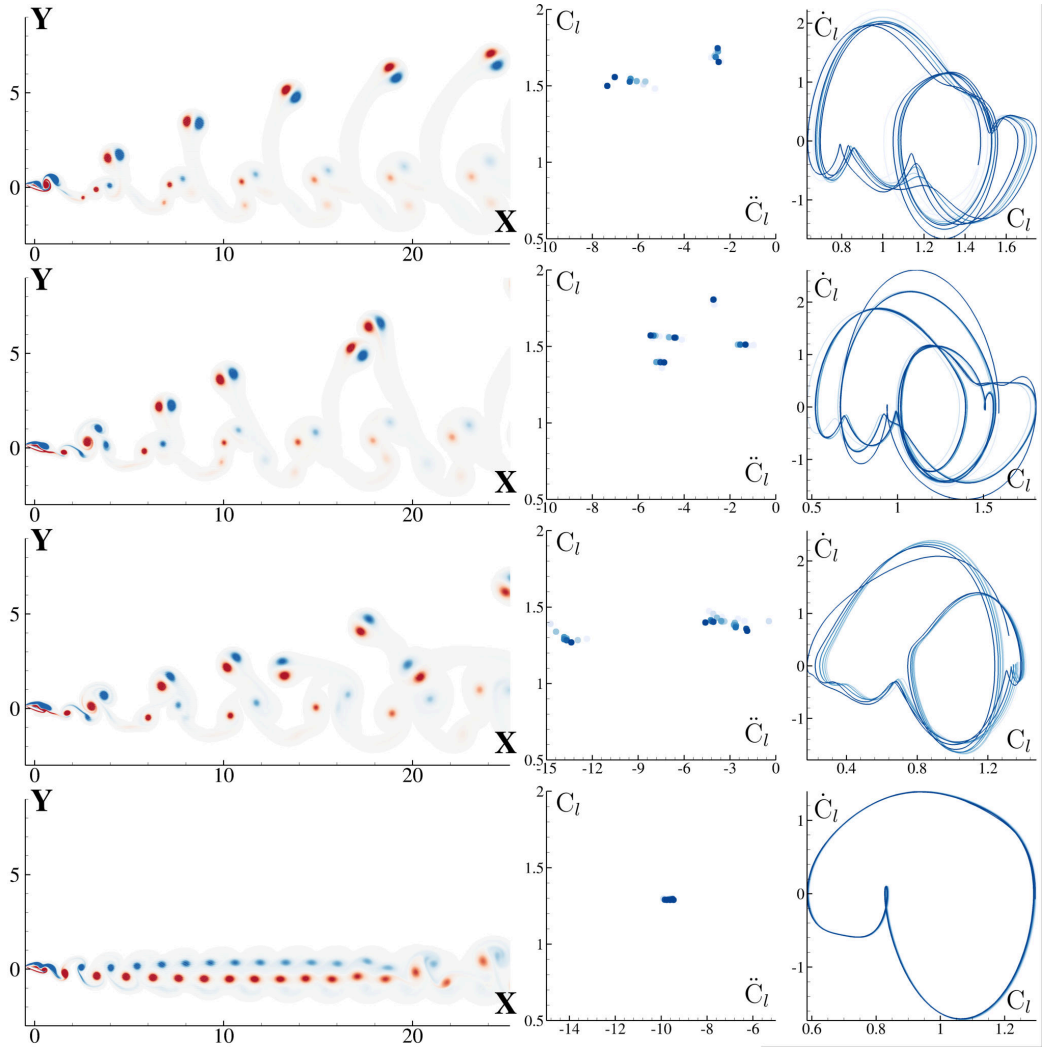


Figure 17. Vorticity fields (**left**), Poincarè sections (**center**) and phase maps (**right**) for $b/a = 0.1$ and $\alpha = 20°$ at Reynolds number 1480. From top to bottom: $t^* = 67.5$, $t^* = 150.0$, $t^* = 181.5$ and $t^* = 300.0$. The non-dimensional time is $t^* = tU/c$, the non-dimensional frequency is $f^* = c/(tU)$. The vorticity is contoured from blue to red for $|\omega| \leq 5$.

In the top row of Figure 18, the lift time signal and the corresponding Fourier transform at $Re = 3000$ are drawn. The signal is clearly periodic although not monochromatic and the spectrum possesses a typical discrete peaks shape, each one representing the higher harmonics of the carrier signal. This case is already discussed in section 5.2 and is here recalled as a reference case. Similarly, the wake field depicted in Figure 19, shows a regular Von Kármán shedding with the vortex patches aligned along the direction connecting the stagnation points on the ellipse and, coherently, one point only is detectable on the corresponding Poincarè section.

When the Reynolds number rises up to 3200, the signal undergoes to a slight frequency modulation that has no evident effects on the signal carrier but is appreciable on the Fourier spectrum. The presence of two other peaks between the main

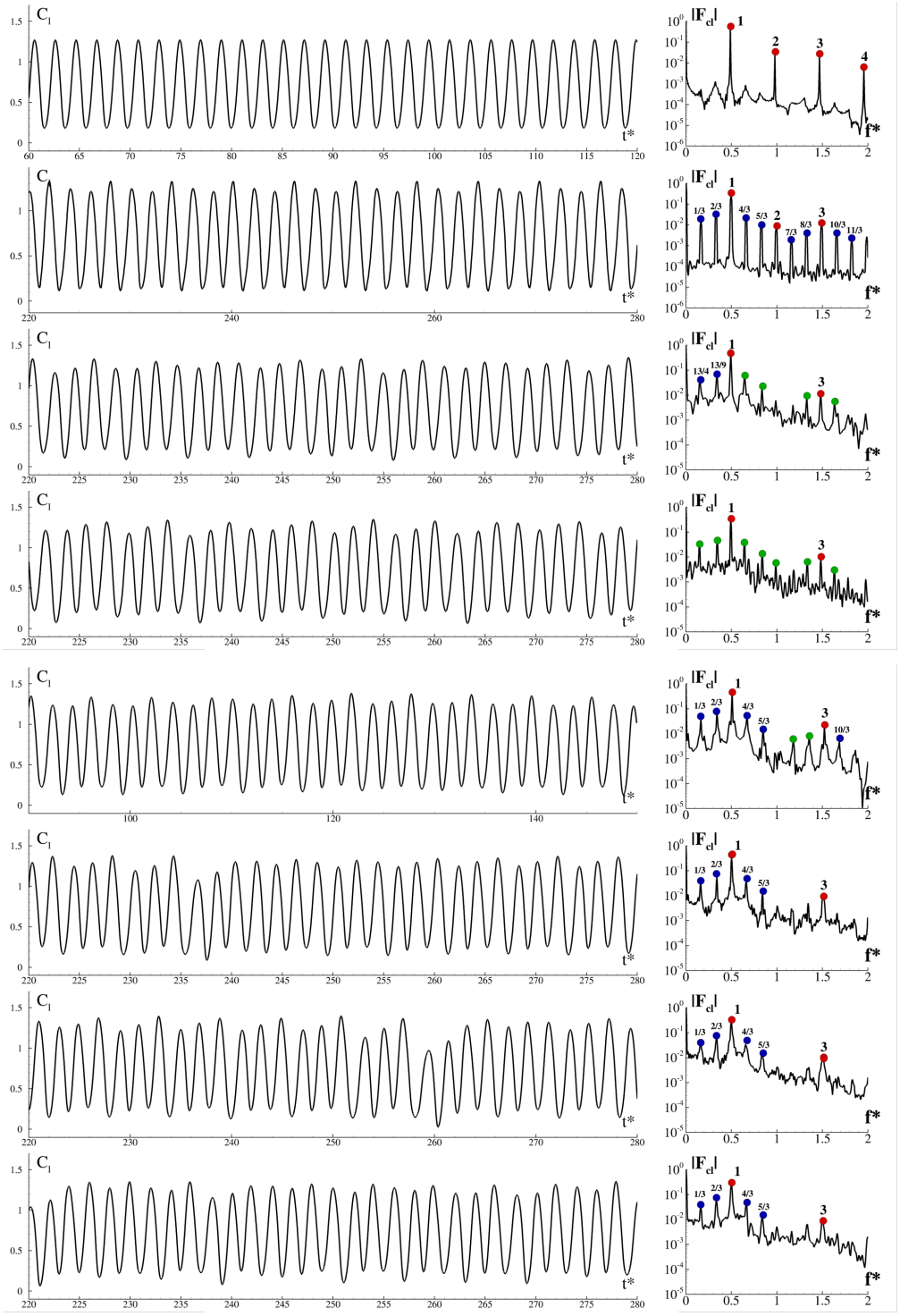


Figure 18. Lift signals (**left**) and related Fourier transforms (**right**) for $b/a = 0.4$ and $\alpha = 20°$ at varying Reynolds number. From top to bottom: $Re = 3000$, $Re = 3200$, $Re = 3500$, $Re = 3800$, $Re = 4000$, $Re = 4100$, $Re = 4200$ and $Re = 4300$. The non-dimensional time is $t^* = tU/c$, the non-dimensional frequency is $f^* = c/(tU)$. The peaks corresponding to the harmonics of the signals are marked with red dots and with the corresponding numbers. With blue dots the peaks of commensurable sub-harmonics are marked and the corresponding fraction is indicated. The non commensurable sub-harmonics peaks are marked with green dots.

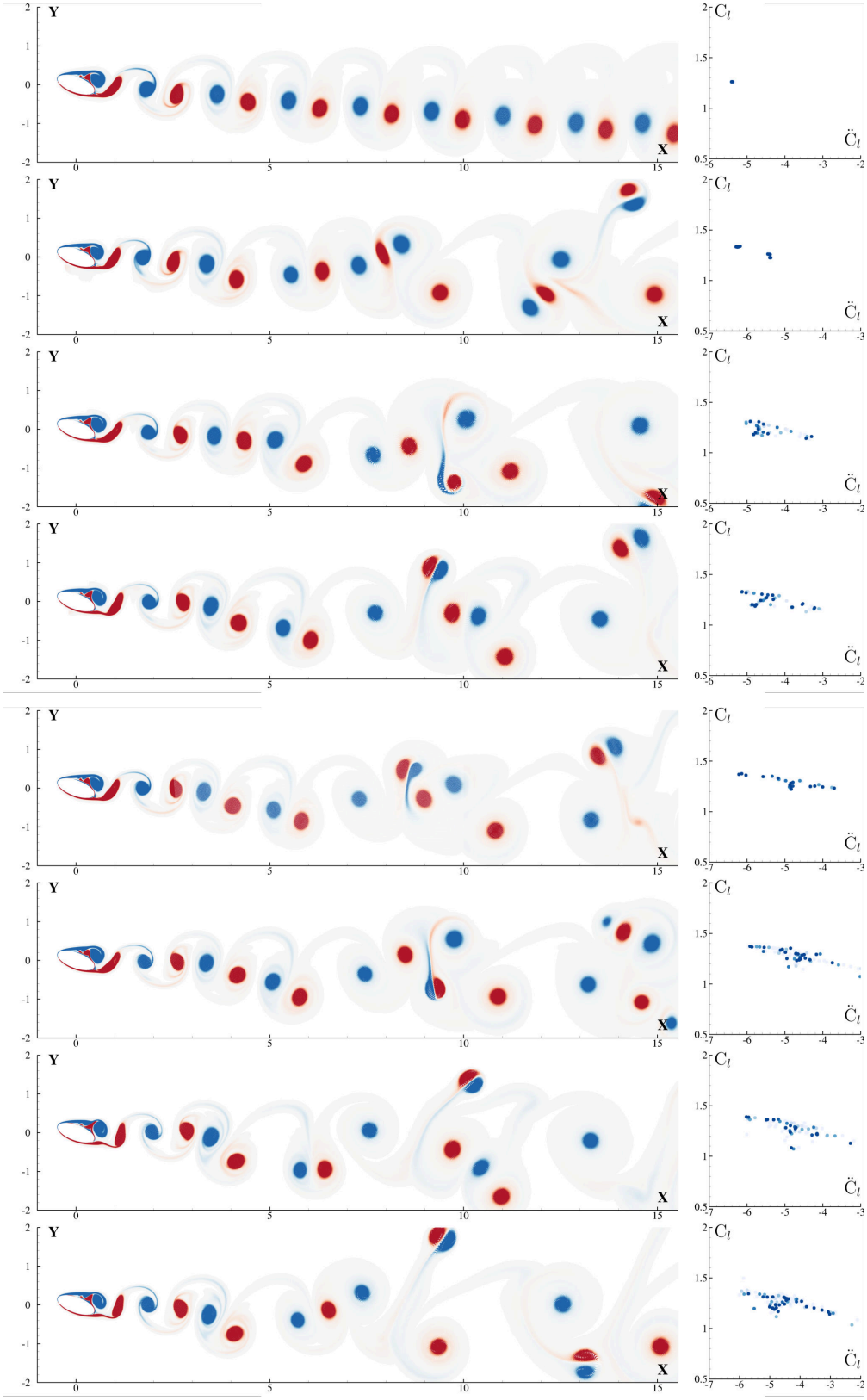


Figure 19. Vorticity fields (**left**) and related Poincarè section (**right**) for $b/a = 0.4$ and $\alpha = 20°$ at varying Reynolds number. From top to bottom: $Re = 3000$, $Re = 3200$, $Re = 3500$, $Re = 3800$, $Re = 4000$, $Re = 4100$, $Re = 4200$ and $Re = 4300$. The vorticity is contoured from blue to red for $|\omega| \leq 5$.

ones of the basic signal (which are actually the same of the case $Re = 3000$) indicates a period-tripling bifurcation. Furthermore, the vorticity field in Figure 19 depicts a near wake (up to 3-5 chords from the body) very similar to the former case, but more interacting vortex dipoles for a distance greater than 7 chords from the ellipse. Due to the close values of two lift maxima in the Poincarè section two point clusters are exhibited rather than three.

By further increasing the Reynolds number, the period-tripling bifurcation becomes more evident with sharp and greater peaks in the Fourier spectrum and a clear signal modulation in the lift time history. In Figure 18 this behaviour is found when the Reynolds number passes from 3200, to 3500 and finally to 3800 where numerous little peaks seems to lead the system toward a new bifurcation. The wake becomes more and more unstable with strong dipoles interaction just after 5 chords, while in the Poincarè sections the lift maxima assume scattered distributions, not evidencing the bifurcations found in the Fourier transforms. This behaviour is essentially related to the fact that, when a blunt body is considered, the signal modulations are significantly weaker than the basic function and the lift maxima variations are rather little within the period, giving this observed "gullwing-like" shape.

The passage of the thickness from $b/a = 0.1$ to $b/a = 0.4$ makes the response of the system to the Reynolds number variation very similar to a blunt body, similarly to the dynamics of the flow past a circle. Higher Reynolds numbers (4000, 4100, 4200 and 4300 are plotted) make the signal even less regular, with a spectrum passing from a discrete peaks fashion to a single leading peak overlying an almost continuous spectrum (*i. e.* see bottom row of Figure 18). During this passage, the signal first exhibits irregular ranges of period-tripling bifurcations alternated to more regular ones (this is the case of $Re = 4000$ and $Re = 4100$), but for highest Reynolds number (4300) the maxima variations during the numerous modulations appear less intense respect to the time signal. This, obviously, does not mean that the system assumes a more ordered configuration in terms of vorticity field and, in fact, the wakes seem more and more irregular and the Poincarè sections are dually even more scattered.

In the next section, we will see that this mechanism will bring the system into a chaotic regime.

## 6 Chaotic regime

When dealing with a chaotic regime in the framework of the flows past rigid bodies, many possible conditions can be accomplished by the fluid flow. By looking at the lift time signal, a chaotic regime refers to a condition for which this signal is chaotic, *i.e.* its Fourier transform does not exhibits typical discrete-peaks spectra, as seen in the previous sections, but a continuous spectrum (as stressed in Durante

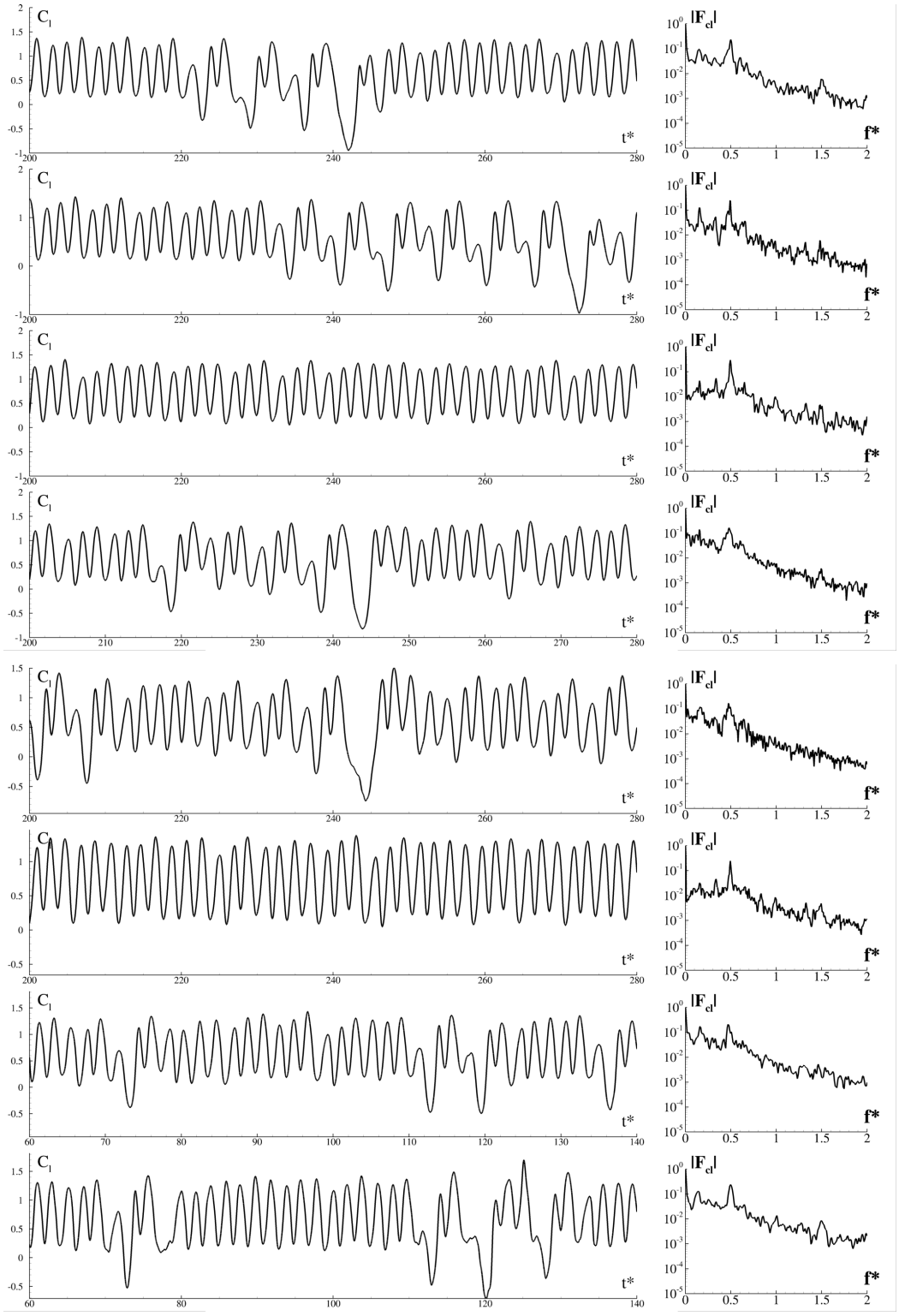


Figure 20. Lift signals (**left**) and related Fourier transforms (**right**) for $b/a = 0.4$ and $\alpha = 20°$ at varying Reynolds number. From top to bottom: $Re = 4400$, $Re = 4500$, $Re = 4600$, $Re = 4700$, $Re = 4800$, $Re = 4900$, $Re = 5000$ and $Re = 6000$. The non-dimensional time is $t^* = tU/c$, the non-dimensional frequency is $f^* = c/(tU)$.

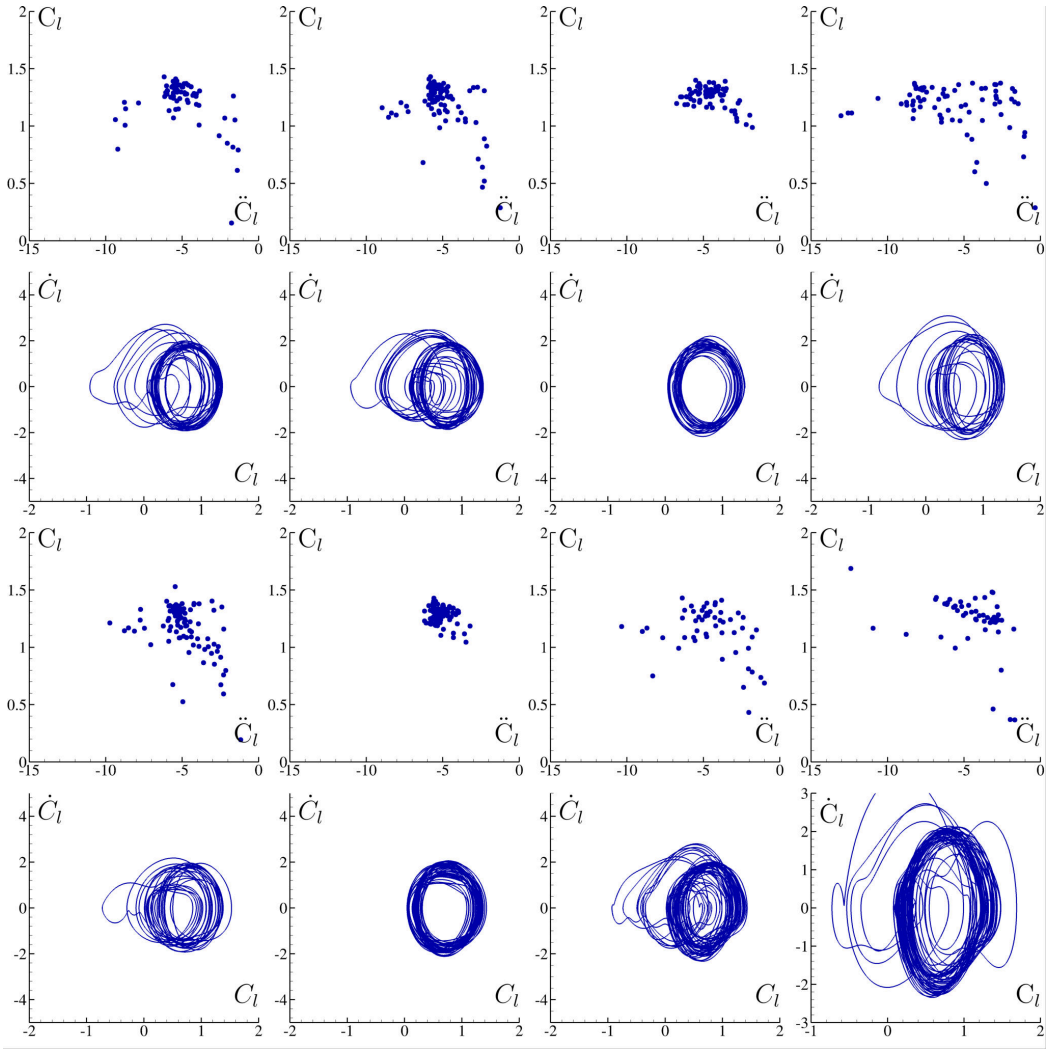

Figure 21. Poincarè sections (**dotted**) and related phase maps (**solid lines**) for $b/a = 0.4$ and $\alpha = 20°$ at varying Reynolds number. From top left to bottom right: $Re = 4400$, $Re = 4500$, $Re = 4600$, $Re = 4700$, $Re = 4800$, $Re = 4900$, $Re = 5000$ and $Re = 6000$.

et al. [11, 12]). In the present study, the chaotic condition is achieved or by an unpredictable modulation of a periodic carrier, or by numerous bifurcations toward different regimes or by a completely irregular signal.

The passage from discrete to continuous of the spectra is the evidence of the route from a periodic regime to a non-periodic one where the frequencies involved belong to a continuous range. Indeed in a periodic regime only a numerable set of frequencies are excited, being them related to the scale of the eddies shed in the wake field. Conversely in the non-periodic regime the vorticity is shed through eddies of different scales.

It is important to stress that, disregarding the excited frequencies in the near wake, the characteristics of the mid/far wake are a consequence of the mutual interactions of the released eddies. This means that the flow field may result as turbulent (in the

classical kinetic energy distribution sense), even though the lift remains a periodic time signal. Moreover, being the present study restricted to a 2D framework, the inverse cascade also plays an important role in the reorganization in big eddies of the shed vorticity. Indeed, if the wake becomes turbulent, the turbulent kinetic energy is distributed over the different vortex scales in such a way that small scales transfer the energy to greater scales (see also Boffetta and Ecke [3]). This mechanism is opposite to the direct energy cascade (which is dominant in 3D framework) where the energy of the larger eddies is transferred to smaller ones.

Because the effect of the angle of attack is essentially to lower the Reynolds number at which the transition to chaotic regime occurs, the present section is focused on the effect of the thickness, for which significant differences in the behaviour of the dynamical system appear (see also table 2).

When dealing with the thick ellipse (*i.e.* $b/a = 0.4$), it is interesting to linger on Figure 20 where the passage from $Re = 4400$ to $Re = 6000$ is shown in terms of the lift signal and its Fourier transform. In the cases $Re = 4400$ and $Re = 4500$ the carrier signal bifurcates unpredictably toward a different state and this is found also in the Fourier spectra, shown in Figure 20. The long persistence of the system on a regime with a regular lift time signal (see for $Re = 4400$ the time intervals $200 < t^* < 220$ or $250 < t^* < 280$, or for $Re = 4500$ the time intervals $200 < t^* < 230$) causes the presence of an evident peak at the shedding frequency of the carrier signal, but the presence of the bifurcations produces a continuous spectrum. The Poincarè sections and phase maps in Figure 21 makes the former discussion more complete and meaningful. The first and second frame on the top left are characterised by an evident cluster of points, which are the maxima of the carrier signal, and other scattered points representing the bifurcation conditions. At $Re = 4400$ the phase map shows a marked nearly circular orbit, indicating that the fundamental regime is rather periodic. A large number of other orbits representing the time signal bifurcations discussed before allows to classify this behaviour as a strange attractor, according to the classical dynamical system theory.

Conversely, at $Re = 4500$, although the Poincarè section is rather similar to the former one, the phase map tells something more: the system is basically shifting between two regimes represented by the two orbits visible in the map.

When the Reynolds number rises to 4600 the system comes back to a more ordered condition. In this case, the lift time signal is not affected by bifurcations, although unpredictable modulations make the Fourier spectrum continuous with one sharp peak (see third frame from top of Figure 20). Similarly, the Poincarè section and the corresponding phase map depicts a single point cluster and a single orbit, obviously not sharp because of the modulations. It is interesting to note how the system is moving toward a chaotic condition: the road is not straight with the Reynolds number increasing, but the system experiences rather direct and inverse routes.

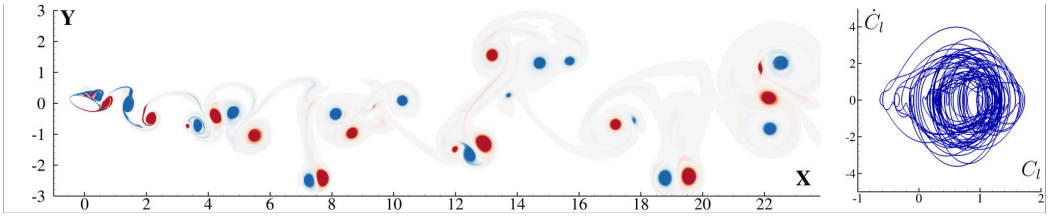


Figure 22. Vorticity field for $b/a = 0.4$ and $\alpha = 20°$ at $Re = 10000$ (**left**) and corresponding phase map (**right**). The non-dimensional vorticity contours are in the range $-4 \leq \omega^* \leq 4$.

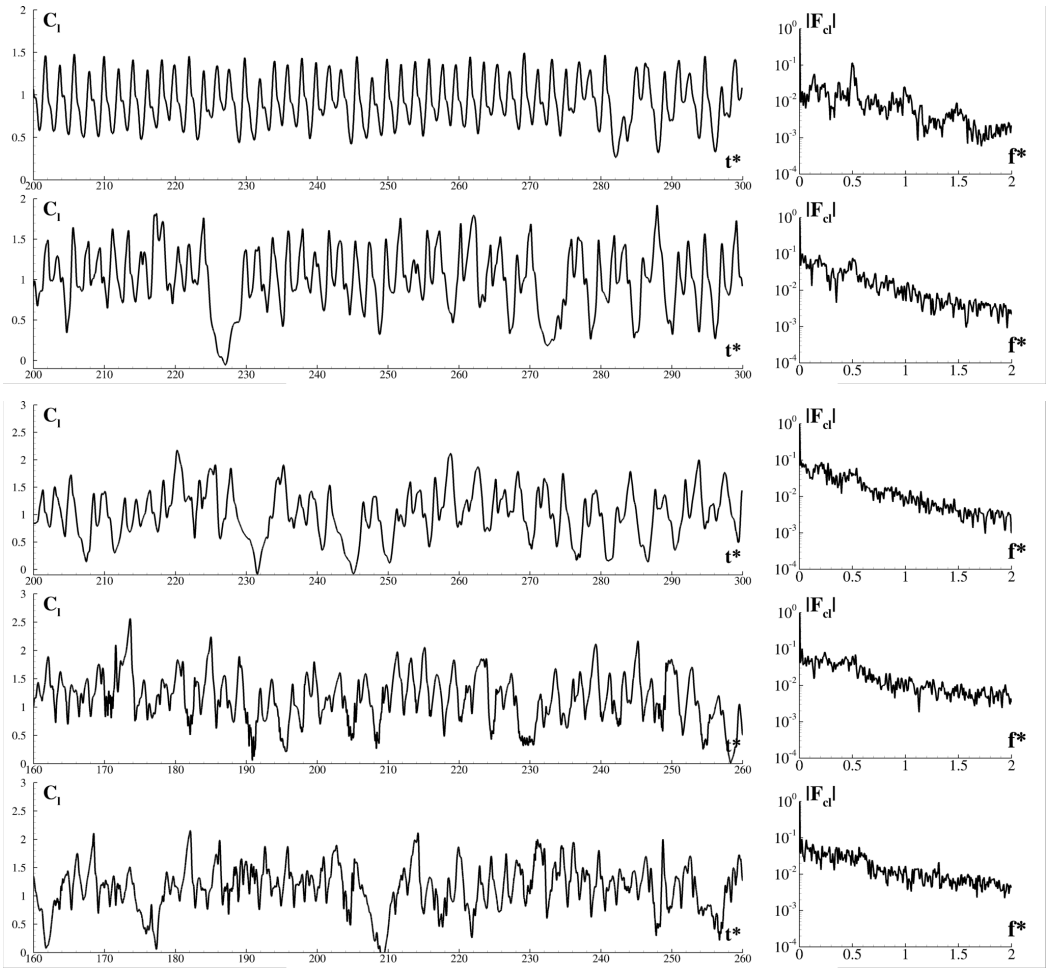


Figure 23. Lift signals (**left**) and related Fourier transforms (**right**) for $b/a = 0.1$ and $\alpha = 20°$ at varying Reynolds number. From top to bottom: $Re = 2000$, $Re = 3000$, $Re = 4000$, $Re = 6000$ and $Re = 10000$. The non-dimensional time is $t^* = tU/c$, the non-dimensional frequency is $f^* = c/(tU)$.

Indeed, increasing further the Reynolds number at 4700 and 4800 the Poincarè sections show again scattered points distributions and numerous orbits in the phase maps (see the corresponding frames in Figure 21). Similarly, the Fourier spectra of the time signals (shown in Figure 20) are almost continuous and the main peaks themself are hardly discernible, conversely to the former cases. When the Reynolds number rises again, at $Re = 4900$, the system comes back to a more regular lift

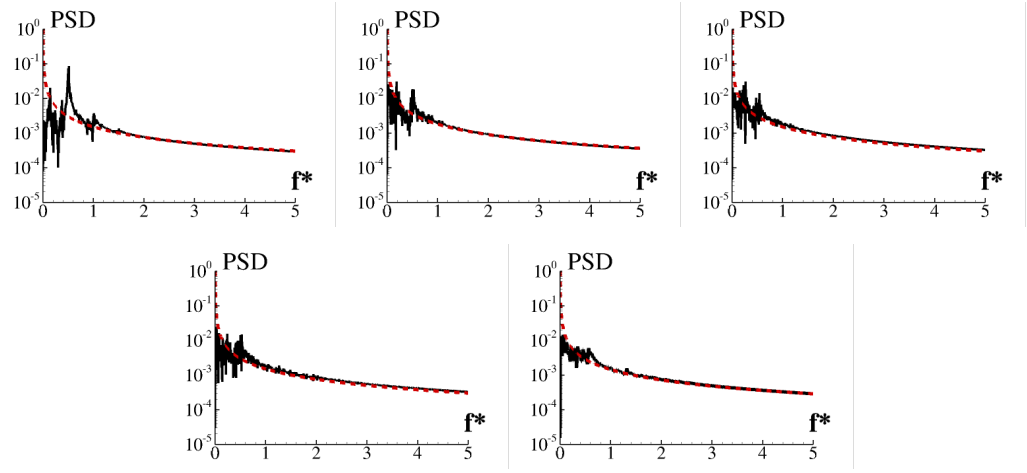


Figure 24. Power spectrum densities (solid) and asymptotic behaviours (dashed) for $b/a = 0.1$ and $\alpha = 20°$ at varying Reynolds number. From top left to bottom right: $Re = 2000$, $Re = 3000$, $Re = 4000$, $Re = 6000$ and $Re = 10000$. The non-dimensional frequency is $f^* = c/(tU)$.

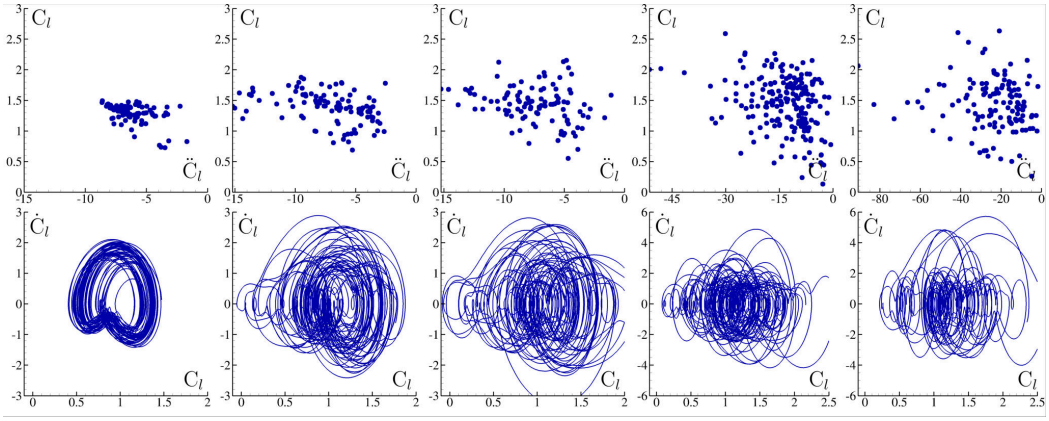


Figure 25. Poincarè sections (**top**) and related phase maps (**bottom**) for $b/a = 0.1$ and $\alpha = 20°$ at varying Reynolds number. From left to right: $Re = 2000$, $Re = 3000$, $Re = 4000$, $Re = 6000$ and $Re = 10000$. The plot intervals of Poincarè sections at $Re = 6000$ and $Re = 10000$ are widened in abscissa to cover the whole range of curvatures.

time signal, with a main evident peak at the shedding frequency in the spectrum and evidently clustered maxima in the Poincarè sections (see the related frame in Figure 21).

Further increases of the Reynolds number bring the dynamical system to a non reversible chaotic condition, as visible in the last frames of Figure 20 and in the Poincarè sections with the corresponding phase maps of Figure 21, where a large number of orbits are obtained. In Figure 22 the case $Re = 10000$ is depicted in terms of the vorticity field and phase map. It patently appears the chaotic nature of the flow field and the orbits' tangle in the related phase map. When the phase map appears as intricate as in this case, a fully chaotic condition is attained. In Figure 27, a similar dynamics is observed for $Re = 10000$, the situation is quite similar, although

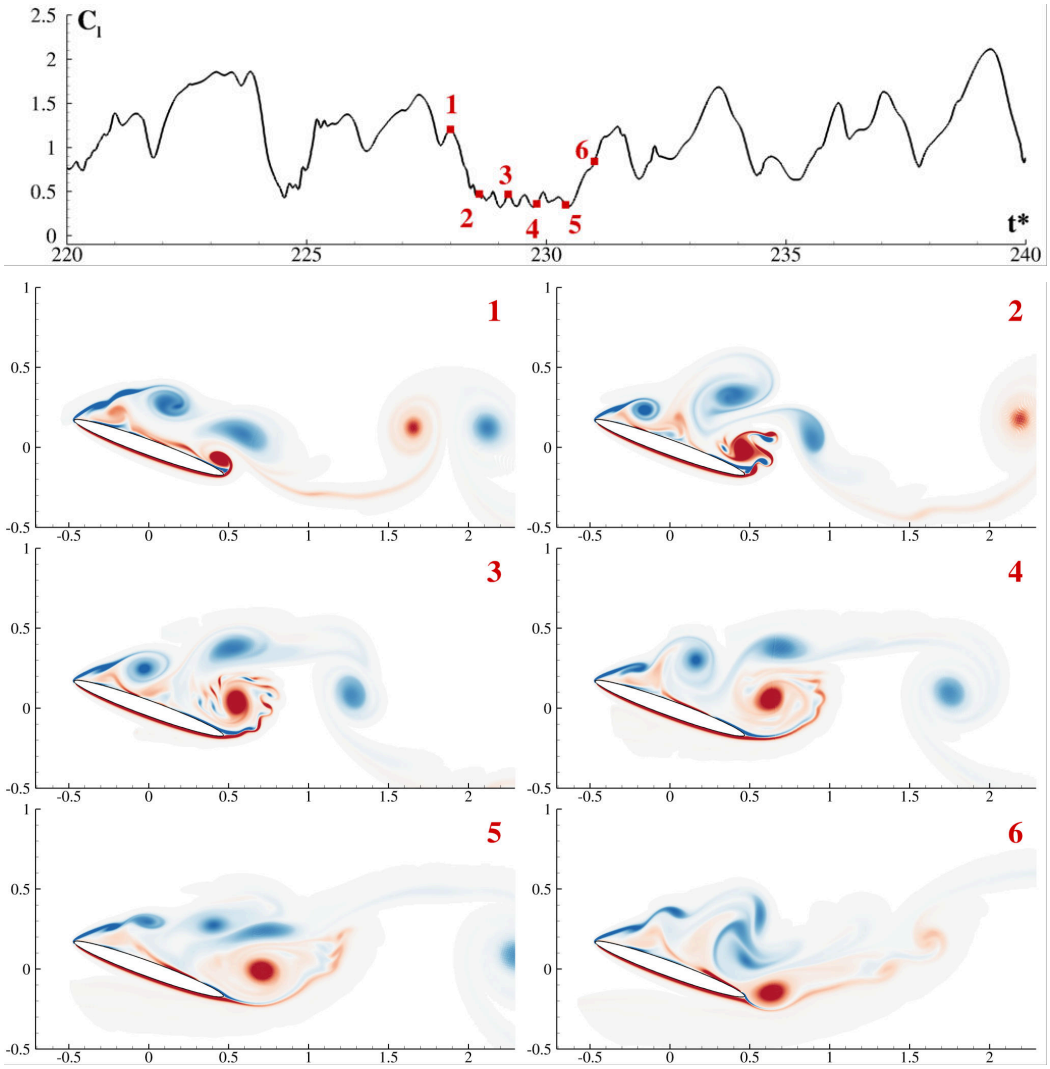


Figure 26. Lift signal for $b/a = 0.1$, $\alpha = 20°$ and $Re = 6000$ with the six time instants highlighted. The non-dimensional time is $t^* = tU/c$. The corresponding vorticity fields are depicted below. The non-dimensional vorticity contours (from blue to red) are in the range $-35 \leq \omega^* \leq 35$.

the increasing of the Reynolds number allows the formation of lower scale eddies, the evidence of which are detectable in the large dipole structure downstream (see frame 1 of Figure 27). The trailing edge vortex is more complex and surrounded by a series of little dipoles making a sort of *necklace* around it. This richness in different scales emerging in correspondence of the airfoil surface is the main responsible of the corresponding chaotic nature of the lift force, discussed before. For $b/a = 0.1$ the system presents a chaotic regime for a significantly lower Reynolds number. From the top frame of Figure 23, the lift time signal at $Re = 2000$ is sketched together with its Fourier transform. The carrier signal is still recognizable and similar to the case $Re = 1450$ seen in the previous section, although affected by a significant irregularity. The spectrum exhibits a rather evident peak, but does not share any similarity with the $Re = 1800$ lastly sketched in the former section. As

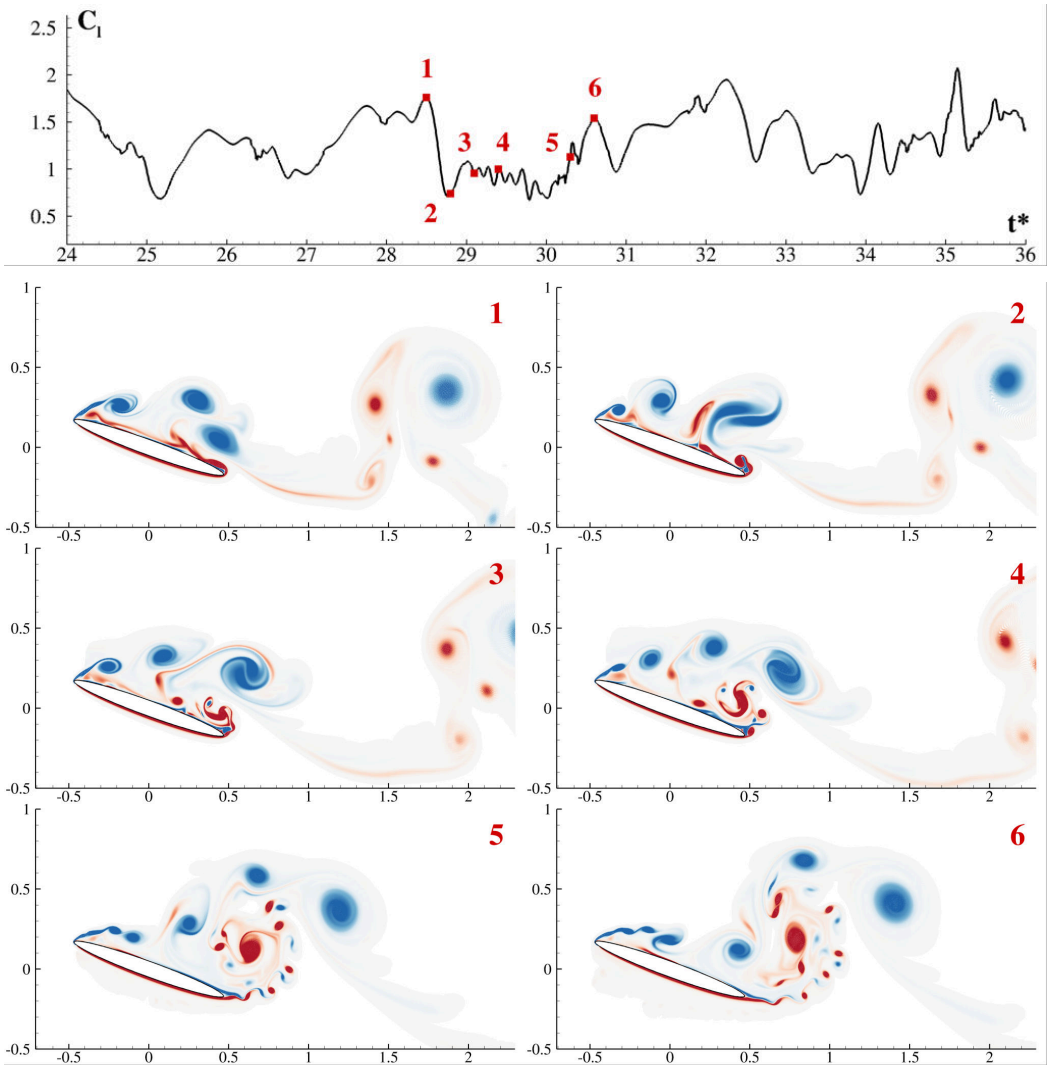


Figure 27. Lift signal for $b/a = 0.1$, $\alpha = 20°$ and $Re = 10000$ with the six time instants highlighted. The non-dimensional time is $t^* = tU/c$. The corresponding vorticity fields are depicted below. The non-dimensional vorticity contours (from blue to red) are in the range $-35 \leq \omega^* \leq 35$.

seen before in the thick ellipse case, the presence of a peak in the Fourier spectrum translates in a significant point clustering in the Poincarè section even in this case (see the corresponding frame of Figure 25) and, coherently, the phase map shows a blurred orbit. From now on, any other Reynolds number increase makes the lift signal so chaotic that the spectrum becomes completely continuous and tilted, at $Re = 10000$, it resembles more to a *pink noise*. This kind of noise is often found in the statistical fluctuations of a wide number of diverse physical and biological systems (see Handel [18]) and it is based on a characteristic behaviour of the power density spectrum (PSD) which assumes a $1/f^{\beta}$ trend with $0 < \beta \leq 2$. In order to get the PSD spectrum, the autocorrelation functions have been deduced from the time signals of Figure 24 and the Wiener-Khinchin theorem have been exploited (for details, see Wiener [48]). As sketched in Figure 24, at $Re = 2000$ a periodic signal

exists for low frequencies, this being visible from the evident peaks for $f^* < 1$, but it assumes the classical pink noise trend $\approx 1/f^*$ with $\beta = 1$ for higher frequencies, highlighted with dashed lines in the frames. A similar situation holds for Reynolds going from 3000 to 6000 where the embedded periodic patterns are even less evident. At $Re = 10000$ the spectrum remains in the trend with $\beta = 1$, but the periodic patterns are rather absent, as expected.

The Poincarè sections, although almost confined in the $C_l$ range, become very scattered along $\ddot{C}_l$ in coherence with the fact that in chaotic conditions the lift time signal experiences larger variations in curvature rather than in amplitude.

In Figures 26 and 27 a different interpretation of the chaotic regime, observed in the thin ellipse case, is proposed in terms of the shed vorticity. In the top frames, a magnification of the lift time signal is drawn together with some interesting time instants sketched below and accordingly numbered.

In both cases, the airfoil works in stalled conditions with an evident separation at the leading edge. The first frame is referred to a lift peak where rather large scale eddies (*i.e.* around one fifth of the chord length) are shed in the wake field. A trailing edge vortex patch bent upstream is visible for $Re = 6000$ case (see Figure 26) and a large dipole at 2 chords of distance is also found. The lift drop observed after the first frame is accompanied by an important instability at the trailing edge where a big vortex with positive vorticity forms and remains displaced in correspondence with the suction side. In the frames 3 and 4 of Figure 26 it becomes clear that the couple of vortices, coming from the leading edge (with negative sign) and from trailing edge (with positive sign), induces a force normal to the airfoil that pushes it downward, implying the observed drop in the lift force. When this trailing edge vortex moves downstream, the lift rises up again (see frame 6 of the same figure and the corresponding point in the lift time signal).

## 7 Global behaviour

In the present section a general discussion on the mean lift coefficient $\overline{C}_l$ variation related to the Reynolds number or to the angle of attack is carried out and discussed according to the simulation matrix presented in section 2.

By considering that the mean lift is zero for all the cases at $\alpha = 0°$, the series N1 (thick case) and N3 (thin case) will not be considered.

The variation of the $\overline{C}_l$ with the Reynolds number related to the series N5 was already shown and commented in Rossi et al. [39] and it will be only recalled but not shown again.

In Figure 28, two frames are related to the thick (series N2) and thin (series N4) cases for $\alpha = 20°$ with remarkable differences between them. As expected, the thick ellipse is less lifting than the thin one with a maximum around 0.72 for a Reynolds number between 3200 and 4600 and without any clear lifting peak. Conversely, the thin ellipse shows a first maximum of 1.22 at $Re = 1500$, suddenly reached from $Re = 1450$ where the lift value is around 0.9, and a second one near $Re = 8000$ where $\overline{C}_l \approx 1.36$. This behaviour is linked to the period bifurcations observed and discussed in section 5.4 and induced by a change in the topology of the wake field which becomes less compact. Similarly, for the thin ellipse at $\alpha = 30°$ (series N5) bifurcations were also found and a lift increase was shown and discussed in Rossi et al. [39]. When the Reynolds number rises to 1700, a new change in the wake topology appears that leads to a regular periodic signal and to a drop in the mean lift. At $Re = 1800$, as discussed in 5.4, the lift signal change again and a new local maximum in the $\overline{C}_l$ is observed (see bottom frame of Figure 28). In the chaotic regime of the thin ellipse, the lift assumes a growing trend up to $Re = 8000$, where a maximum is attained. At the present stage, a final explanation of the $\overline{C}_l$ behaviour within the chaotic regime is still lacking and should be further investigated.

In the case of the thick ellipse, top frame of Figure 28, the trend seems more flat and not evident changes in the global behaviour are found in the passage from periodic to chaotic regime. Furthermore, a little drop is observed at $Re = 4700$ although it is not clearly related to a wake change. It is worth to underline that for the thick ellipse, the error bars representing the RMS (Root Mean Square) of the time signal are rather wide, both in the periodic and chaotic regime regions, if compared to the corresponding thin case. In this latter, indeed, the variance of the signal is more confined in the periodic region, whereas it increases in the chaotic one, as expected. Conversely, the thick ellipse, being more similar to a blunt body, experiences larger amplitudes in the lift signal, this implying more intense load vibrations induced by the shedding.

More clear is the behaviour of the lift respect to the angle of attack, coming from series N6 and N7 and depicted in Figure 29, leaving the airfoil shape unaltered ($b/a = 0.1$). At $Re = 2000$ (left frame, related to series N6) the lift grows until a maximum is attained at 15°, after which the separation moves to the leading edge and the profile becomes fully stalled. At this point, the lift manifests a little drop and starts to grow again almost up to 45°, where the drag overcomes the lift and the profile behaves actually as an obstacle within the flow field (see also Durante et al. [12]). After the maximum is reached, the lift decreases to zero (almost linearly) until $\alpha = 90°$.

For the lower Reynolds number case $Re = 250$ (series N7), the situation is significantly different. The lift trend is bell shaped with a linear behaviour up to 15°. The growing up to 45° is here moderate and the situation does not change evidently up to 60°, where it starts to lower as in the former case.

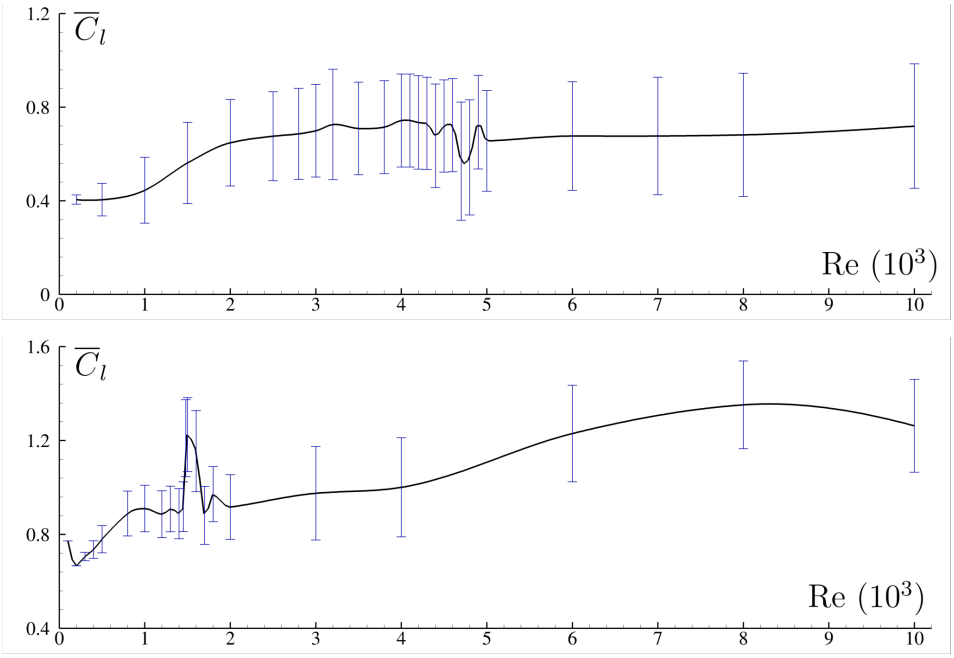


Figure 28. Mean lift coefficient behaviour with the Reynolds number for cases of series N2 (**top**) and N4 (**bottom**). With vertical lines the error bars related to the root mean square of the corresponding time signals.

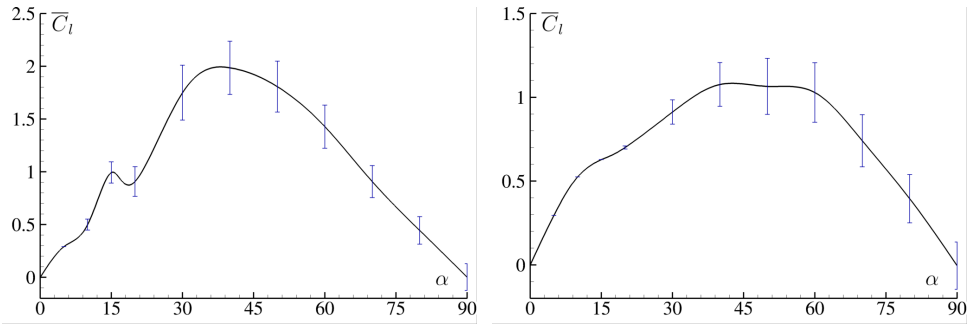


Figure 29. Mean lift coefficient behaviour with the angle of attack (in degrees) for cases of series N6 (Re=2000) (**left**) and N7 (Re=250) (**right**). With vertical lines, the error bars related to the root mean square of the corresponding time signals.

Concluding, a synoptic table indicating all the regimes found for all the Series investigated is reported in table 2.

## 8 Conclusions

In the present paper an analysis of the 2D flow past an elliptic cylinder is carried out. Highly resolved simulations have been performed with a Vortex Particle Method, called DVH, which is based on the solution of the Helmholtz equation through the Chorin's operator splitting approach. By solving only the vortical part of the flow

| N1 | 0° | B/A=0.4 |
|---|---|---|
| Re | | REGIME |
| 200 | | Steady |
| 500 | *M* | Periodic |
| 1000 | *M* | Periodic |
| 1500 | *M* | Periodic |
| 2000 | *Q-P* | Periodic |
| 2500 | *NM* | Periodic |
| 3000 | *Q-P* | Periodic |
| 4000 | *Q-P* | Periodic |
| 5000 | *Q-P* | Periodic |
| 6000 | *Q-P* | Periodic |
| 7000 | *Q-P* | Periodic |
| 8000 | *Q-P* | Periodic |
| 10000 | *Q-P* | Periodic |

| N2 | 20° | B/A=0.4 |
|---|---|---|
| Re | | REGIME |
| 100 | | Steady |
| 200 | *M* | Periodic |
| 500 | *NM* | Periodic |
| 1000 | *NM* | Periodic |
| 1500 | *NM* | Periodic |
| 2000 | *NM* | Periodic |
| 2500 | *NM* | Periodic |
| 2800 | *NM* | Periodic |
| 3000 | *NM* | Periodic |
| 3200 | *SH* | Periodic |
| 3500 | *SH* | Periodic |
| 3800 | *SH* | Periodic |
| 4000 | *SH* | Periodic |
| 4100 | *SH* | Periodic |
| 4200 | *SH* | Periodic |
| 4300 | *SH* | Periodic |
| 4400 | | Chaotic |
| 4500 | | Chaotic |
| 4600 | | Chaotic |
| 4700 | | Chaotic |
| 4800 | | Chaotic |
| 4900 | | Chaotic |
| 5000 | | Chaotic |
| 6000 | | Chaotic |
| 7000 | | Chaotic |
| 8000 | | Chaotic |
| 10000 | | Chaotic |

| N3 | 0° | B/A=0.1 |
|---|---|---|
| Re | | REGIME |
| 500 | | Steady |
| 1000 | | Steady |
| 2000 | | Steady |
| 3000 | | Steady |
| 4000 | | Steady |
| 5000 | | Steady |
| 6000 | | Steady |
| 7000 | *M* | Periodic |
| 8000 | *Q-P* | Periodic |
| 10000 | *Q-P* | Periodic |

| N4 | 20° | B/A=0.1 |
|---|---|---|
| Re | | REGIME |
| 100 | | Steady |
| 200 | *M* | Periodic |
| 300 | *NM* | Periodic |
| 400 | *NM* | Periodic |
| 500 | *NM* | Periodic |
| 800 | *NM* | Periodic |
| 1000 | *NM* | Periodic |
| 1200 | *NM* | Periodic |
| 1300 | *NM* | Periodic |
| 1400 | *SH* | Periodic |
| 1450 | *SH* | Periodic |
| 1480 | *SH* | Periodic |
| 1500 | *SH* | Periodic |
| 1600 | *SH* | Periodic |
| 1700 | *SH* | Periodic |
| 1800 | *SH* | Periodic |
| 2000 | | Chaotic |
| 3000 | | Chaotic |
| 4000 | | Chaotic |
| 6000 | | Chaotic |
| 8000 | | Chaotic |
| 10000 | | Chaotic |

| N5 | 30° | B/A=0.1 |
|---|---|---|
| Re | | REGIME |
| 100 | *M* | Periodic |
| 250 | *NM* | Periodic |
| 500 | *NM* | Periodic |
| 600 | *NM* | Periodic |
| 700 | *NM* | Periodic |
| 800 | *NM* | Periodic |
| 900 | *NM* | Periodic |
| 950 | *SH* | Periodic |
| 1000 | *SH* | Periodic |
| 1100 | *SH* | Periodic |
| 1200 | *SH* | Periodic |
| 1300 | | Chaotic |
| 1400 | | Chaotic |
| 1500 | | Chaotic |
| 1550 | | Chaotic |
| 1600 | | Chaotic |
| 1650 | | Chaotic |
| 1700 | | Chaotic |
| 1800 | | Chaotic |
| 1900 | | Chaotic |
| 1400 | | Chaotic |

| N6 | Re=2000 | B/A=0.1 |
|---|---|---|
| α | | REGIME |
| 0° | | Steady |
| 5° | | Steady |
| 10° | *M* | Periodic |
| 15° | *NM* | Periodic |
| 20° | | Chaotic |
| 30° | | Chaotic |
| 40° | | Chaotic |
| 50° | | Chaotic |
| 60° | | Chaotic |
| 70° | | Chaotic |
| 80° | *Q-P* | Periodic |
| 90° | *Q-P* | Periodic |

| N7 | Re=250 | B/A=0.1 |
|---|---|---|
| α | | REGIME |
| 0° | | Steady |
| 5° | | Steady |
| 10° | | Steady |
| 15° | | Steady |
| 20° | *M* | Periodic |
| 30° | *NM* | Periodic |
| 40° | *NM* | Periodic |
| 50° | *NM* | Periodic |
| 60° | *Q-P* | Periodic |
| 70° | *NM* | Periodic |
| 80° | *NM* | Periodic |
| 90° | *NM* | Periodic |

Table 2
Schematic diagram of regime transitions for the all the test series. Every regime is highlighted with a different color. The periodic regimes are specified as follows: M - monochromatic, NM - non-monochromatic, Q-P - quasi-periodic, SH - sub-harmonics.

field, this method allows to achieve Direct Numerical Simulation like resolutions at reasonable computational costs.

The investigation was focused on the identifications of different regimes that lead the lift time signal from steady to chaotic behaviour, considering two different thickness, variable angle of attack and variable Reynolds numbers. To this purpose long-time simulations were carried out, in order to attain the identified regime within a wide enough time range.

Period-doubling bifurcations was discovered and commented in terms of Fourier spectra, Poincarè sections and phase maps for the thin case. In the thick case, this mechanism is less dramatic and this reflects to the Poincarè sections as commented in section 6. Furthermore, in some scenario, bifurcations were also observed during the transients (see section 5.4).

Significant differences between thin and thick ellipse chaotic regimes were documented and the presence of a "pink noise" behaviour of the lift time signal in the thin case was discovered.

Another important aspect of the present analysis is the investigation in terms of the vorticity flow fields which has been connected to the time behaviour of the lift force, where meaningful.

The present investigation may be extended to higher Reynolds numbers, for different thickness and angles of attack. Indeed, at Re of order $10^5$ turbulent transition of the boundary layer is expected to affect the forces on the body.

**Acknowledgments**

The research activity was developed within the Project Area "Applied Mathematics" of the Department of Engineering, ICT and Technology for Energy and Transport (DIITET) of the Italian National Research Council (CNR).

## A Brief description of the numerical scheme

In this section, the main characteristics of the vortex particle method used for solving the fluid motion equations are presented. The method is called Diffused Vortex Hydrodynamics (DVH) and further details can be found in Colagrossi et al. [7], Durante et al. [11, 12], Giannopoulou et al. [14], Rossi et al. [36, 37, 38, 39].

The governing equations are the Navier–Stokes equations describing the motion of

an incompressible fluid which are rewritten in vorticity formulation:

$$\begin{cases} \dfrac{D\mathbf{u}}{Dt} = -\dfrac{\nabla p}{\rho_0} + \nu\nabla^2\mathbf{u} \\ \\ \nabla \cdot \mathbf{u} = 0 \end{cases} \qquad \Rightarrow \qquad \frac{D\omega}{Dt} = \nu\,\nabla^2\omega \tag{A.1}$$

where the $D/Dt$ is the Lagrangian time derivative. The vorticity formulation of the above equations is solved through an operator splitting based on an advection step and a diffusion steps, according to Chorin [5].

In a 2D framework the advection step is:

$$\begin{cases} \dfrac{D\omega}{Dt} = 0 \\ \\ \dfrac{D\mathbf{r}}{Dt} = \mathbf{u}(\mathbf{r}, t) \end{cases} \qquad \text{with} \qquad \nabla^2\mathbf{u} = -\nabla \times \boldsymbol{\omega} \tag{A.2}$$

where $\mathbf{u}(\mathbf{r}, t)$ is the velocity field of the material point $\mathbf{r}$ at time $t$ and $\boldsymbol{\omega} = \omega\,\mathbf{e}_3$ being $\mathbf{e}_3$ the unitary vector orthogonal to the flow plane. The right term in Equation (A.2) is the Poisson equation linking the vorticity with the velocity field.

By exploiting the Helmholtz-Hodge Decomposition, the velocity field is decomposed in a curl-free (potential) part $\mathbf{u}_\phi$ and a divergence-free (non potential) part $\mathbf{u}_\omega$. The velocity component due to the free stream $\mathbf{u}_\infty$ is also added to $\mathbf{u}_\phi$. The $\mathbf{u}_\omega$ component is obtained through the Biot-Savart law in a 2D framework for an unbounded domain. Indeed this law is a free solution of the Poisson Equation (A.2). The enforcement of the impermeability boundary condition on the body surface $\partial\Omega_B$ is performed with the $\mathbf{u}_\phi$ solution using an Indirect Boundary Element Method (IBEM). The IBEM solution also provide the circulation density distribution $\gamma$ used to enforce the no-slip condition on the solid boundary during the diffusion step (see Cottet [9], Chorin et al. [6]).

The latter consists in the diffusion of the vorticity due to the viscosity which is a phenomenon governed by the linear heat equation:

$$\begin{cases} \partial_t\omega = \nu\nabla^2\omega, & \mathbf{r} \in \Omega \\ \\ \nu\dfrac{\partial\omega}{\partial n} = -\dot{\gamma}, & \mathbf{r} \in \partial\Omega_B \end{cases} \tag{A.3}$$

the time variation of the circulation density $\gamma$ on $\partial\Omega_B$ becomes a source term and it is diffused into the flow as part of the existing vorticity field (for details see Giannopoulou et al. [14]).

In order to discretize the above PDEs, the vorticity field is described in terms of a

collection of $N_v$ discrete vortices as:

$$\omega(\mathbf{r}, t) = \sum_{j=1}^{N_v} \Gamma_j(t)\, \zeta_\epsilon(\mathbf{r} - \mathbf{r}_j(t)), \tag{A.4}$$

where $\Gamma_j$ is the circulation of the $j$-th particle and $\zeta_\epsilon$ is the kernel function, which is a smoothed Dirac function with parameter $\epsilon > 0$.

### *A.1 Computational Costs*

The total number of simulations performed for this work is 121 (see table 2). The number of vortex particles spans between 150,000 and 2,500,000 from the lowest Reynolds number up to the highest, while the number of time iteration ranges between 7000 to 70,000. The simulations used in this work have been all performed on 8 cluster nodes (2×18-core Intel Xeon E5-2697 v4 2.30GHz). The CPU costs of the implemented algorithm for 2D cases are about 100 $\mu s$ per vortex particle and per time iteration on a single core. In order to perform the 121 simulations the time requested on the 8 cluster nodes was about 40 days. This cost is inline with other vortex particle solvers and it is grossly affected by the Fast Multipole Method for the solution of the Poisson Equation (A.2).

## B Some remarks on the link between force and vorticity

According to Equation (4), the forces are evaluated through the time derivative of the sum of the circulations of all the vortices shed in the wake field, multiplied by the vertical or horizontal component of their position.

This means that the effect of the whole flow field is taken into account when the force time signals are investigated.

A typical misconception about it, is the common assumption that the force behaviour is mainly connected with the near field dynamics, being with the medium/far field almost irrelevant. This is not correct and, in order to clarify this point to a less expert reader, a sample case is taken into account.

An impulsively started steady current flowing past an airfoil, like a NACA0012, is considered for a small profile incidence.

Top plot of Figure B.1 depicts the vorticity field shed by a NACA0012 with $\alpha = 6°$ and the Reynolds number set to 10000. The field is calculated at time $t = 3.5c/U$, being $c$ the airfoil chord length. As highlighted in the figure, the vorticity distribution is almost steady within the near field $\Omega_1$, *i.e.* $\partial\omega/\partial t \simeq 0$. Conversely, in

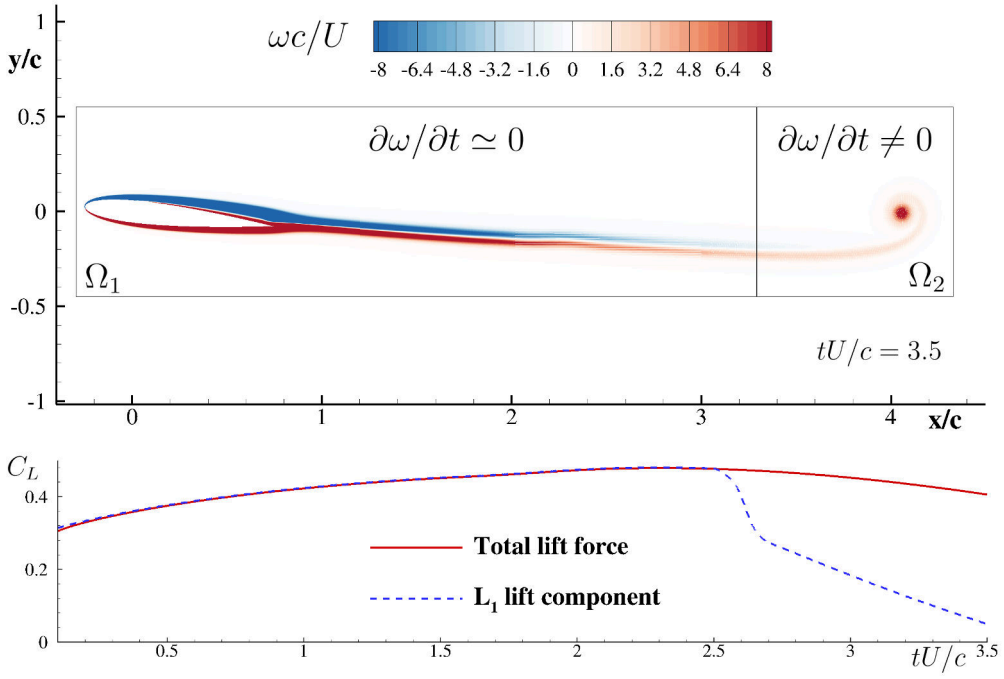


Figure B.1. Flow past a NACA0012 airfoil at angle of attack of 6° due to an impulsively started steady current. **Top**: vorticity field at non-dimensional time $tU/c = 3.5$ and Reynolds number 10000. **Bottom**: time history of the lift coefficient evaluated in $\Omega$ (solid line) and in $\Omega_1$ only (dashed).

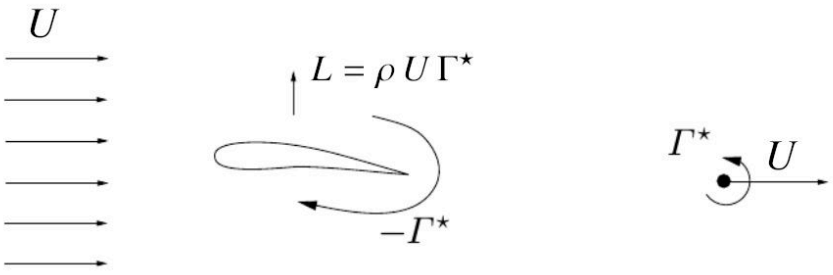


Figure B.2. Sketch of the inviscid flow past an airfoil according to the Kutta-Joukowski theorem.

the farther field $\Omega_2$ the starting vortex moves rightward at rather the free stream velocity, so that $\partial\omega/\partial t \neq 0$.

On the bottom plot of the same figure, the time history of the lift force is reported. Following the Equation (3), the vertical force is given by:

$$L = \rho \int_\Omega x \frac{\partial \omega}{\partial t}\, dV = \underbrace{\rho \int_{\Omega_1} x \frac{\partial \omega}{\partial t}\, dV}_{L_1} + \underbrace{\rho \int_{\Omega_2} x \frac{\partial \omega}{\partial t}\, dV}_{L_2} \tag{B.1}$$

The solid line is the lift force $L$, whereas the dashed line is the contribution $L_1$, coming from the vorticity in $\Omega_1$ domain only. The curves are superimposed as far

as the wake is in $\Omega_1$. For non-dimensional time $tU/c > 2.5$, the wake enters in $\Omega_2$ and the component $L_1$ quickly decreases towards zero.

According to the former considerations, it follows that the lift behaviour is due to the vorticity time variation, related to the starting vortex motion. Indeed, even if the intensity of the vorticity and its time derivative decreases in the far field, the Formula (B.1) ensures that its effect, being weighted with the horizontal position, is anyway important.

As explained in Section 3, when using a Particle Vortex Method the lift force is calculated through the summation:

$$L = \rho \frac{d}{dt} \left( \sum_{j=1}^{N_v(t)} x_j(t) \, \Gamma_j(t) \right) \tag{B.2}$$

In potential flow theory the above equation may be further simplified, by considering a single vortex with circulation $\Gamma^\star$, shed at initial time and moving downstream with the stream velocity $U$ (see Figure B.2). The lift force comes from the well-known Kutta-Joukowski theorem:

$$L = \rho \frac{d}{dt} \left( x^\star(t) \, \Gamma^\star \right) = \rho \, U \, \Gamma^\star \tag{B.3}$$

## References


[1] G. Bailador, G. Trivino, and A. Van der Heide. Fuzzy sets of quasiperiodic signals. In *XIV Congreso espanol sobre tecnologıa y lógica fuzzy (ESTYLF 2008)*, 2008.

[2] G. K. Batchelor. *An introduction to fluid dynamics*. Cambridge university press, 2000.

[3] G. Boffetta and R. E. Ecke. Two-dimensional turbulence. *Annual Review of Fluid Mechanics*, 44:427–451, 2012.

[4] Chandan Bose and Sunetra Sarkar. Investigating chaotic wake dynamics past a flapping airfoil and the role of vortex interactions behind the chaotic transition. *Physics of fluids*, 30(4):047101, 2018.

[5] A. J. Chorin. A numerical method for solving incompressible viscous flow problems. *Journal of computational physics*, 2(1):12–26, 1967.

[6] A. J. Chorin, T. J.R. Hughes, M. F. McCracken, and J. E. Marsden. Product formulas and numerical algorithms. *Communications on Pure and Applied Mathematics*, 31(2):205–256, 1978.

[7] A. Colagrossi, E. Rossi, S. Marrone, and D. Le Touzé. Particle Methods for Viscous Flows: Analogies and Differences Between the SPH and DVH Methods. *Communications in Computational Physics*, 20(3):660–688, 2016.

[8] Andrea Colagrossi, Giorgio Graziani, and Mario Pulvirenti. Particles for flu-

ids: Sph versus vortex methods. *Mathematics and Mechanics of complex systems*, 2(1):45–70, 2014.

[9] G.H. Cottet. Boundary conditions and deterministic vortex methods for the navier-stokes equations. In *Mathematical aspects of vortex dynamics*, pages 128–143, 1989.

[10] G.H. Cottet, P. D. Koumoutsakos, et al. *Vortex methods: theory and practice*. Cambridge university press, 2000.

[11] D. Durante, E. Rossi, A. Colagrossi, and G. Graziani. Numerical simulations of the transition from laminar to chaotic behaviour of the planar vortex flow past a circular cylinder. *Communications in Nonlinear Science and Numerical Simulation*, 48:18–38, 2017.

[12] D. Durante, E. Rossi, and A. Colagrossi. Bifurcations and chaos transition of the flow over an airfoil at low Reynolds number varying the angle of attack. *Communications in Nonlinear Science and Numerical Simulation*, page 105285, 2020.

[13] F. B. Fonseca, S. S. Mansur, and E. Del Rio Vieira. Flow around elliptical cylinders in moderate reynolds numbers. In *Proceedings of the 22nd international congress of mechanical engineering, November*, pages 3–7, 2013.

[14] O. Giannopoulou, A. Colagrossi, A. Di Mascio, and C. Mascia. Chorins approaches revisited: Vortex particle method vs finite volume method. *Engineering Analysis with Boundary Elements*, 106:371388, 2019.

[15] R. Gilmore. Topological analysis of chaotic dynamical systems. *Reviews of Modern Physics*, 70(4):1455, 1998.

[16] S. Goldstein. On laminar boundary-layer flow near a position of separation. *The Quarterly Journal of Mechanics and Applied Mathematics*, 1(1):43–69, 1948.

[17] G. Graziani and P. Bassanini. Unsteady viscous flows about bodies: Vorticity release and forces. *Meccanica*, 37(3):283–303, 2002.

[18] P. H. Handel. The nature of fundamental 1/f noise. *AIP Conference Proceedings*, 285(1):162–171, 1993.

[19] CP Jackson. A finite-element study of the onset of vortex shedding in flow past variously shaped bodies. *Journal of fluid Mechanics*, 182:23–45, 1987.

[20] S. A. Johnson, M. C. Thompson, and K. Hourigan. Predicted low frequency structures in the wake of elliptical cylinders. *European Journal of Mechanics-B/Fluids*, 23(1):229–239, 2004.

[21] M Saif Ullah Khalid and Imran Akhtar. Characteristics of flow past a symmetric airfoil at low reynolds number: A nonlinear perspective. In *ASME 2012 International Mechanical Engineering Congress and Exposition*, pages 167–175. American Society of Mechanical Engineers, 2012.

[22] D. F. Kurtulus. On the unsteady behavior of the flow around naca 0012 airfoil with steady external conditions at re= 1000. *International Journal of Micro Air Vehicles*, 7(3):301–326, 2015.

[23] D. F. Kurtulus. On the wake pattern of symmetric airfoils for different incidence angles at re= 1000. *International Journal of Micro Air Vehicles*, 8(2): 109–139, 2016.

[24] Yan Liu, Kailun Li, Jiazhong Zhang, Hang Wang, and Liguang Liu. Numerical bifurcation analysis of static stall of airfoil and dynamic stall under unsteady perturbation. *Communications in Nonlinear Science and Numerical Simulation*, 17(8):3427–3434, 2012.

[25] SC Luo, TT Lim, KB Lua, HT Chia, EK R. Goh, and QW Ho. Flowfield around ogive/elliptic-tip cylinder at high angle of attack. *AIAA journal*, 36 (10):1778–1787, 1998.

[26] M. T. Nair and T.K. Sengupta. Onset of asymmetry: flow past circular and elliptic cylinders. *International Journal for Numerical Methods in Fluids*, 23 (12):1327–1345, 1996.

[27] Jin Koo Park, Seung O Park, and Jae Min Hyun. Flow regimes of unsteady laminar flow past a slender elliptic cylinder at incidence. *International Journal of Heat and Fluid Flow*, 10(4):311–317, 1989.

[28] L. Pasquale, D. Durante, and R. Broglia. Flow separation prevention around a NACA0012 profile through multivariable feedback controlled plasma actuators. *Computers & Fluids*, 182:85–107, 2019.

[29] I Paul, K Arul Prakash, S Vengadesan, and V Pulletikurthi. Analysis and characterisation of momentum and thermal wakes of elliptic cylinders. *Journal of Fluid Mechanics*, 807:303–323, 2016.

[30] Immanuvel Paul, K Arul Prakash, and S Vengadesan. Onset of laminar separation and vortex shedding in flow past unconfined elliptic cylinders. *Physics of Fluids*, 26(2):023601, 2014.

[31] Thomas H Pulliam and John A Vastano. Transition to chaos in an open unforced 2d flow. *Journal of Computational Physics*, 105(1):133–149, 1993.

[32] B. R. Ramaprian and B. G. Shivaprasad. The structure of turbulent boundary layers along mildly curved surfaces. *Journal of Fluid Mechanics*, 85(2):273–303, 1978.

[33] J Bala Bhaskara Rao and V Ramachandra Raju. Numerical and heat transfer analysis of shell and tube heat exchanger with circular and elliptical tubes. *International Journal of Mechanical and Materials Engineering*, 11(1):6, 2016.

[34] G. Riccardi and D. Durante. *Elementi di fluidodinamica: Un'introduzione per l'Ingegneria*. Springer Science & Business Media, 2007.

[35] GJ Richards. On the motion of an elliptic cylinder through a vicous fluid. *Philosophical Transactions of the Royal Society of London. Series A, Containing Papers of a Mathematical or Physical Character*, 233(721-730):279–301, 1934.

[36] E Rossi, A Colagrossi, B Bouscasse, and G Graziani. The Diffused Vortex Hydrodynamics method. *Communications in Computational Physics*, 18(2): 351–379, 2015.

[37] E Rossi, A Colagrossi, and G Graziani. Numerical Simulation of 2D-Vorticity Dynamics using Particle Methods. *Computers and Mathematics with Applications*, 69(12):1484–1503, 2015.

[38] E. Rossi, A. Colagrossi, D. Durante, and G. Graziani. Simulating 2d viscous flow around geometries with vertices through the diffused vortex hydrodynamics method. *Computer Methods in Applied Mechanics and Engineer-*

*ing*, 302:147–169, 2016.

[39] E Rossi, A Colagrossi, G Oger, and D LeTouzé. Multiple bifurcations of the flow over stalled airfoils changing the Reynold numbers. *Journal of Fluid Mechanics*, 846:356–391, 2018.

[40] Arun K Saha, K Muralidhar, and G Biswas. Transition and chaos in two-dimensional flow past a square cylinder. *Journal of engineering mechanics*, 126(5):523–532, 2000.

[41] S. Sen and S. Mittal. A study on the far wake of elliptic cylinders. *Computer Modeling in Engineering & Sciences*, 113(1):35–55, 2017. ISSN 1526-1506.

[42] M. Serra and G. Haller. Forecasting long-lived lagrangian vortices from their objective eulerian footprints. *Journal of Fluid Mechanics*, 813:436–457, 2017.

[43] M. Serra, J. Vétel, and G. Haller. Exact theory of material spike formation in flow separation. *Journal of Fluid Mechanics*, 845:51–92, 2018.

[44] K. Shintani, A. Umemura, and A. Takano. Low-reynolds-number flow past an elliptic cylinder. *Journal of Fluid Mechanics*, 136:277289, 1983.

[45] S. P. Singh and S. Mittal. Flow past a cylinder: shear layer instability and drag crisis. *International Journal for Numerical Methods in Fluids*, 47(1):75–98, 2005. doi: 10.1002/fld.807.

[46] PN Sun, A Colagrossi, S Marrone, and AM Zhang. Detection of lagrangian coherent structures in the sph framework. *Computer Methods in Applied Mechanics and Engineering*, 305:849–868, 2016.

[47] Sadatoshi Taneda. Visual study of unsteady separated flows around bodies. *Progress in Aerospace Sciences*, 17:287–348, 1977.

[48] N. Wiener. *Time Series*. M.I.T. Press, 1964. ISBN 9780262230025.

[49] Alan Wolf, Jack B Swift, Harry L Swinney, and John A Vastano. Determining lyapunov exponents from a time series. *Physica D: Nonlinear Phenomena*, 16(3):285–317, 1985.

[50] M. M. Zdravkovich. *Flow around circular cylinders: Fundamentals*, volume 1. Oxford university press, 1997.